Politecnico di Torino

Master of Science in Mechanical Engineering

A.a. 2025/2026

Graduation Session July 2026

Structural and Thermal Analysis of the Port Thermal Shield of the Divertor Tokamak Test (DTT)

Relatori:

Roberto Bonifetto

Giorgio Zavarise

Giulio Ventura

Mauro Corrado

Candidato:

Gautham Gopakumar Thamarassery

Abstract

The Divertor Tokamak Test (DTT) facility, under construction at ENEA Frascati, is an Italian tokamak project conceived to address the plasma exhaust challenge, a key obstacle identified in the European Fusion Roadmap toward the realisation of DEMO. Among its critical subsystems, the Thermal Shield (THS) is a barrier against radiative and conductive heat transfer from the warm tokamak components to the superconducting magnet system operating at 4.5 K. This thesis presents a thermo-mechanical finite element analysis of the DTT Port Thermal Shield (PTS), for structural integrity and to inform design optimisation. The state-of-the-art, ITER and JT-60SA thermal shields are reviewed, whose design philosophies and analytical strategies provide the methodological foundation for the present work.

A computationally efficient FE model was developed in ANSYS Mechanical, informed by prior analyses of the DTT Vacuum Vessel Thermal Shield. The PTS is gravity-supported on the port structure through G10-CR fiberglass epoxy bolts, providing mechanical coupling alongside electrical and thermal insulation. Port and PTS components were discretised using shell elements (SHELL181), while the gravity bolts were represented by beam elements (BEAM188), with temperature-dependent material properties incorporated for both Stainless Steel 316LN and G10-CR. The structural response of the assembly were comprehensively investigated under both gravity and thermal loading conditions.

Structural performance was assessed through total displacement fields, von Mises stress distributions, and inter-component relative gaps, evaluated against allowable criteria. Structural integrity of the PTS assembly is verified under all considered load cases. While the present study successfully characterises the global structural response, more refined local models are recommended in future work to accurately resolve local stress states and support further optimisation of the DTT thermal shield design.

Acknowledgements

The completion of this thesis would not have been possible without the support and encouragement of many people, to whom I owe my sincere gratitude. First and foremost, I would like to thank my supervisors, Prof. Giorgio Zavarise, Prof. Roberto Bonifetto, Prof. Mauro Corrado, and Prof. Giulio Ventura, for their invaluable guidance, patience, and constant support throughout the development of this work. Their expertise and constructive feedback were instrumental in shaping both the technical content and the overall quality of this thesis.

I would also like to express my sincere gratitude to Danilo Acquesta Nunes, doctoral student, for his constant guidance, availability, and technical support throughout the course of this thesis, and to Mohammad Bagheri, my thesis partner, for the collaboration, discussions, and mutual support throughout this journey. Their insights, patience, and companionship made the challenges of this work much easier to navigate. I would also like to extend my sincere appreciation to the DTT team at ENEA for their work on this project, which provided the foundation and context for this thesis.

I wish to express my heartfelt gratitude to my parents, whose unconditional love, sacrifices, and unwavering belief in me have been the foundation of every achievement in my life. Their constant encouragement gave me the strength to pursue my studies far from home and to persevere through every challenge along the way. To my sister, thank you for your constant support, your patience, and for always being there whenever I needed you, near or far. I would also like to thank all my teachers and professors, both from Politecnico di Torino and from my earlier academic journey, whose lessons and mentorship have shaped my growth as an engineer and as a person.

Finally, to my friends, thank you for the countless moments of encouragement, laughter, and support that made this journey memorable. Your presence made even the most demanding days lighter. To everyone who, in one way or another, contributed to this milestone: thank you.

Table of Contents

List of Tables

List of Figures

Chapter 1

Introduction

According to the Global Energy Review 2025 by IEA the world's energy demand rose by 2.2% in 2024, reaching nearly 650 EJ – faster than the average rate over the past decade. Electricity demand grew more rapidly than both overall energy demand and GDP, increasing by 4.3% in 2024. The absolute increase in demand was the largest ever recorded (excluding the jumps in years when the global economy recovered from recession). This reflects structural trends such as growing access to electricity-intensive appliances like air conditioning and a shift towards electricity-intensive manufacturing, as well as increasing power demand from digitalisation, data centers and AI, and the increasing electrification of end-uses. Nearly all the rise in electricity demand was met by low-emissions sources, led by the record-breaking expansion of solar PV capacity, with further growth in other renewables and nuclear power. In 2024, over 7 GW of nuclear power capacity was brought online – 33% more than in 2023.

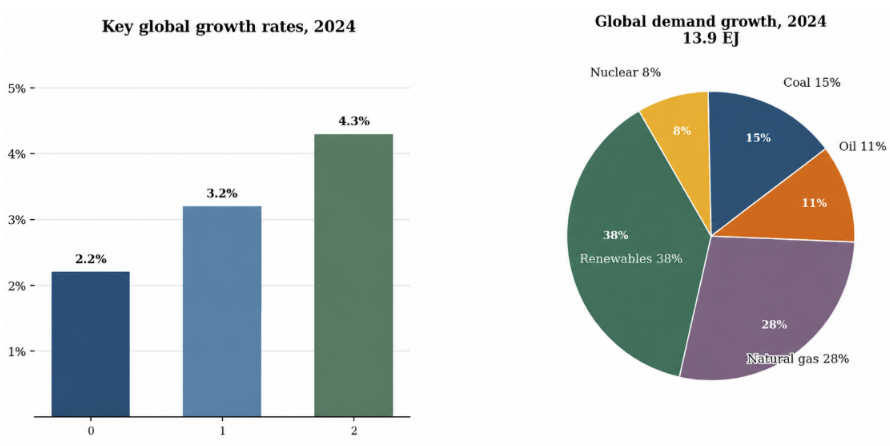

Figure 1.1: Global energy demand growth rate

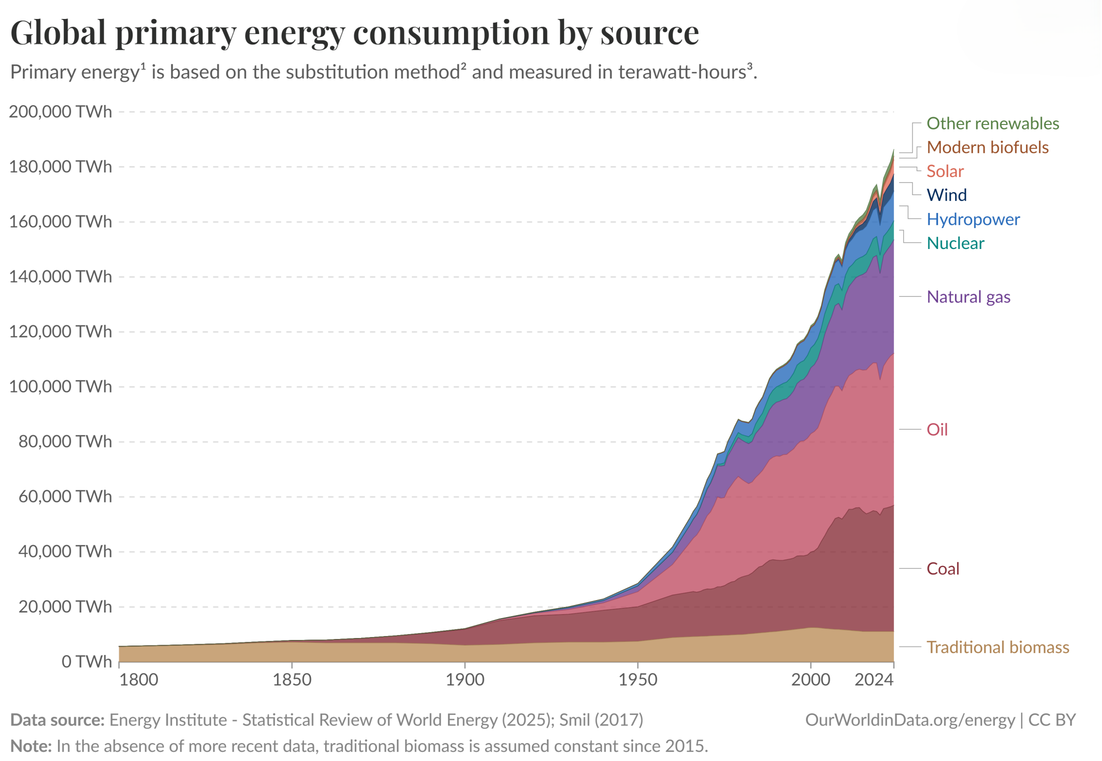

Figure 1.2: Global energy mix

The global energy mix continues to be dominated by fossil fuels, with oil holding the largest share, followed by coal and natural gas. Despite the rapid progress and increasing significance of renewable and low-carbon energy sources such as hydroelectric power, nuclear energy, and other renewables, their share remains comparatively modest. Changing this dependence is critical to cut down on greenhouse gas emissions. Once harnessed, fusion has the potential to be a nearly unlimited, safe and CO2-free energy source.

Humanity has always strived to find energy sources that are cheap, reliable, and abundant. Achieving this would enable nations to become energy independent, eliminating a major source of international tension and conflict over resources. It will help us to address the challenges of climate change and unlock opportunities previously limited by high energy costs, such as large-scale water desalination. Ultimately, it would bring us closer to becoming a Type I civilization. Since the dawn of life, humanity has existed under the reign of a single, distant star. The Sun is far more than a celestial body; it is the foundational engine of our planetary system. What ancient civilizations worshipped as a deity, we now understand through physics as nature's ultimate fusion reactor: a stellar forge where hydrogen nuclei fuse under extreme pressure and temperature, releasing tremendous energy. Nuclear fusion represents not merely the primary power source of our solar system but also a promising avenue for transforming global energy production

1.1 Advantages of Nuclear Fusion

Abundant energy: Fusing atoms together in a controlled way releases nearly four million times more energy than a chemical reaction such as the burning of coal, oil or gas and four times as much as nuclear fission reactions (at equal mass).

Clean and green: Fusion doesn't emit harmful substances like carbon dioxide or other greenhouse gases into the atmosphere. Its major by-product is helium: an inert, non-toxic gas.

Limitless Fuel Supply: Fusion requires two elements: deuterium and tritium. Deuterium can be distilled from all forms of water, while tritium will be produced during the fusion reaction as fusion neutrons interact with lithium. (Terrestrial reserves of lithium would permit the operation of fusion power plants for more than 1,000 years, while sea-based reserves of lithium, used in a fusion reactor in its Li-6 isotope form, would fulfil needs for millions of years.) A critical challenge is how to breed and recover tritium reliably in a fusion device.

No long-lived radioactive waste: Nuclear fusion reactors produce no high activity, long-lived nuclear waste. The activation of components in a fusion reactor is anticipated to be low enough for the materials to be recycled or reused within 100 years, depending on the materials used in the "first-wall" facing the plasma.

Limited risk of proliferation: Fusion doesn't employ fissile materials like uranium and plutonium. (Radioactive tritium is neither a fissile nor a fissionable material.) There are no enriched materials in a fusion reactor that could be exploited to make nuclear weapons.

No risk of meltdown: A Fukushima-type nuclear accident is not possible in a tokamak fusion device. It is difficult enough to reach and maintain the precise conditions necessary for fusion—if any disturbance occurs, the plasma cools within seconds and the reaction stops. The quantity of fuel present in the vessel at any one time is enough for a few seconds only, and there is no risk of a chain reaction.

The ideal future energy mix for the planet would be based on a variety of generation methods instead of a large reliance on one source. As a new source of carbon-free baseload electricity, producing no long-lived radioactive waste, fusion could make a positive contribution to the challenges of resource availability, reduced carbon emissions, and fission waste disposal and safety issues [1].

1.2 Nuclear Fusion

Atoms are always in random motion: the hotter they are, the faster they move. In the Sun's core where temperatures reach 15 million °C, hydrogen atoms are in a constant state of agitation. As they collide at very high speeds, the natural electrostatic repulsion that exists between the positive charges of their nuclei is overcome and the atoms fuse. The fusion of light hydrogen atoms produces a heavier element, helium. This mass deficit is manifested as the release of a considerable quantity of energy, a phenomenon governed by the principle of mass-energy equivalence formalized in Einstein's equation, $E=mc^2$. In this formulation, the energy yield (E) of the fusion reaction is equivalent to the mass defect (m) multiplied by the square of the speed of light (c^2). The magnitude of c^2 acts as a constant of proportionality, ensuring that even a minute reduction in mass results in a profound release of energy.

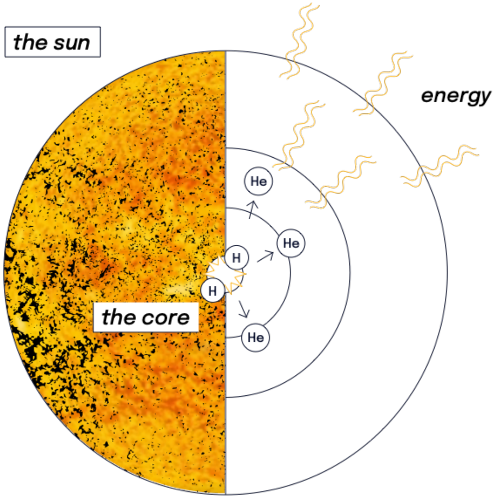

Figure 1.3: Nuclear fusion in the sun

Every second, our Sun turns 600 million tonnes of hydrogen into helium, releasing an enormous amount of energy. But without the benefit of gravitational forces at work in our universe, achieving fusion on Earth has required a different approach.

At extreme temperatures, electrons are separated from nuclei, and a gas becomes a plasma—an ionized state of matter similar to a gas. Composed of charged particles (positive nuclei and negative electrons), plasmas are very tenuous environments, nearly one million times less dense than the air we breathe. Fusion plasmas provide an environment in which light elements can fuse and yield energy. Three conditions must be fulfilled to achieve fusion in a laboratory:

1. very high temperature (to provoke high-energy collisions); fusion reactions require temperatures more than 100 million degrees. To achieve these remarkable temperatures, three separate heating systems are usually used in tokamaks, each capable of delivering well over a million watts of power to the fuel. Together, they generate and sustain plasma that is easily hot enough for the high-energy collisions required for fusion to occur.

2. sufficient plasma particle density (to increase the likelihood that collisions do occur); The constituents of a 100 million-degree plasma are moving about fast, and, if left alone, would soon be so far apart as to render collisions extremely unlikely. To keep the density of the plasma high enough to ensure collisions do occur, the plasma vessel is surrounded by huge electromagnets. These create magnetic fields 10,000 times stronger than the Earth's magnetic field and confine the plasma to circulate within the ring-shaped vessel perpetually. However, if the plasma gets too dense, then collisions of a different kind – between nuclei and electrons – begin to create large amounts of radiation. This radiation, called bremsstrahlung, saps energy from the plasma and prevents fusion from occurring – the optimum density value is around one millionth of the atmosphere.

3. sufficient confinement time (to hold the plasma, which has a propensity to expand, within a defined volume). 80% of the fusion energy is carried away by the neutrons, but the 20% carried by the helium nuclei remains in the plasma. The newly formed helium ricochets around the vessel colliding with unburnt fuel nuclei, heating them up, thereby reducing the need for the external heating systems. However, it takes time for this to happen – depending on the density and temperature of the plasma. The length of time for which particles are confined within the plasma is denoted by τ (the Greek letter tau). Typical current values at JET are on the order of a second, and at ITER should be around four seconds.

At present, two main experimental approaches are being studied: magnetic confinement and inertial confinement. The first method uses strong magnetic fields to contain the hot plasma. The second involves compressing a small pellet containing fusion fuel to extremely high densities using strong lasers or particle beams. A range of magnetized target fusion systems are also being developed, along with experiments with hybrid fusion.

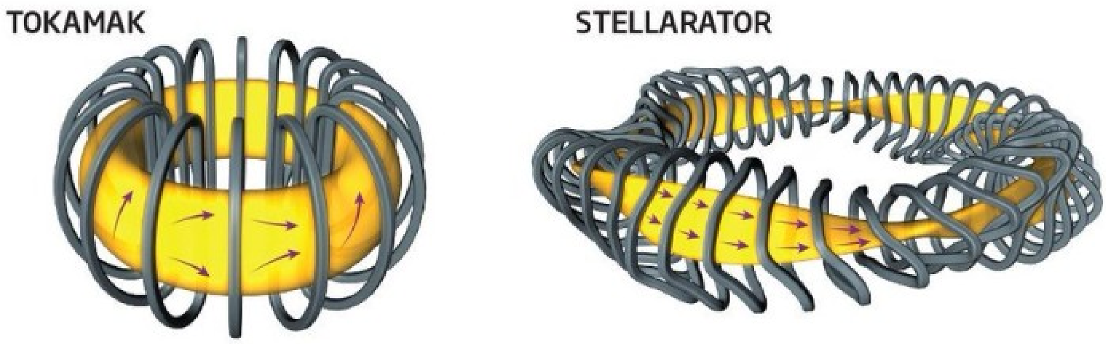

Figure 1.4: Most studied Magnetic confinement concepts: Tokamak & Stellarator

Twentieth-century fusion science identified the most efficient fusion reaction in the laboratory setting to be the reaction between two hydrogen (H) isotopes deuterium (D) and tritium (T). The DT fusion reaction produces the highest energy gain at the "lowest" temperatures. It requires nonetheless temperatures of 150,000,000 degrees Celsius—ten times higher than the hydrogen reaction occurring in the Sun.

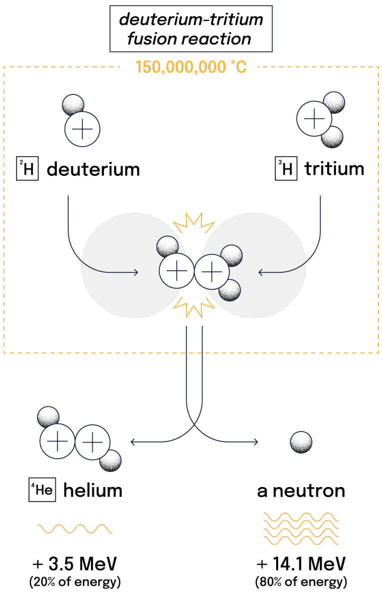

Figure 1.5: Deuterium-Tritium fusion reaction

Each D-T fusion event releases 17.6 MeV (2.8 x 10-12 joule, compared with 200 MeV for a U-235 fission and 3-4 MeV for D-D fusion). On a mass basis, the D-T fusion reaction releases over four times as much energy as uranium fission. Deuterium occurs naturally in seawater (30 grams per cubic metre), which makes it very abundant relative to other energy resources. Tritium occurs naturally only in trace quantities (produced by cosmic rays) and is radioactive, with a half-life of around 12 years. Usable quantities can be made in a conventional nuclear reactor, or in the present context, bred in a fusion system from lithium. Lithium is found in large quantities (30 parts per million) in the Earth's crust and in weaker concentrations in the sea. In a fusion reactor, the concept is that neutrons generated from the D-T fusion reaction will be absorbed in a blanket containing lithium which surrounds the core. The lithium is then transformed into tritium (which is used to fuel the reactor) and helium. In a fusion reactor, the concept is that neutrons generated from the D-T fusion reaction will be absorbed in a blanket containing lithium, which surrounds the core. The lithium is then transformed into tritium (which is used to fuel the reactor) and helium.

$$\mathbf{{}^{6}_{3}Li + {}^{1}_{0}n \longrightarrow {}^{3}_{1}H + {}^{4}_{2}\,He + 4.8\ MeV}$$

$$\mathbf{{}^{7}_{3}Li + {}^{1}_{0}n \longrightarrow {}^{3}_{1}H + {}^{4}_{2}\,He + {}^{1}_{0}n' - 2.5\ MeV}$$

Figure 1.6: Tritium breeding

The blanket must be thick enough (about 1 metre) to slow down the high-energy (14 MeV) neutrons. The kinetic energy of the neutrons is absorbed by the blanket, causing it to heat up. The heat energy is collected by the coolant (water, helium or Li-Pb eutectic) flowing through the blanket and, in a fusion power plant, this energy will be used to generate electricity by conventional methods. An inadequate tritium breeding ratio necessitates external sources, such as producing it in fission reactors. Conversely, any surplus tritium presents significant challenges for handling, storage, and transportation due to its radioactivity and ability to diffuse through materials. The difficulty has been to develop a device that can heat the D-T fuel to a high enough temperature and confine it long enough so that more energy is released through fusion reactions than is used to get the reaction going [1].

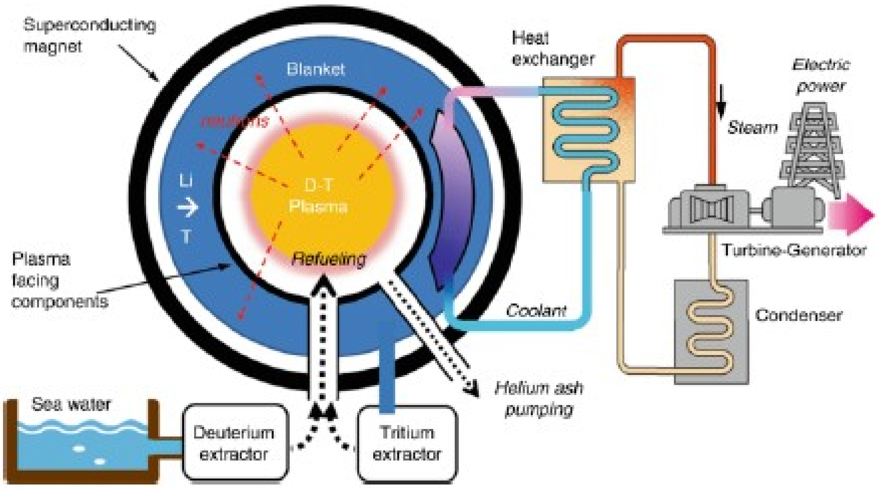

Figure 1.7: schematic diagram of a fusion power plant

1.3 Path to Fusion

1920-1930: Understanding the stars and the atom

Following Eddington's paper, Robert d'Escourt Atkinson and Fritz Houtermans provided the first calculations of the rate of nuclear fusion in stars. And at the same time, Ernest Rutherford was exploring the structure of the atom. With his famous 1934 experiment, Rutherford showed the fusion of deuterium into helium and observed that "an enormous effect was produced" during the process. His student Mark Oliphant used an updated version of the equipment, firing deuterium rather than hydrogen and discovered helium-3 and tritium, showing that heavy hydrogen nuclei could be made to react with each other. This was the first direct demonstration of fusion in the lab. This understanding of nuclear fusion was tied together by Hans Bethe's work on stellar nucleosynthesis where he described that it is through proton-proton chain reactions that the Sun and stars release energy.

1950s: Enter the fusion machines

By the 1950s, researchers started looking at possibilities of replicating the process of nuclear fusion on Earth. And in 1950 soviet scientists Andrei Sakharov and Igor Tamm proposed the design for a type of magnetic confinement fusion device, the tokamak. This was followed, in 1951, by Lyman Spitzer's concept for the stellarator. The stellarator concept dominated fusion research throughout the 1950s but lost its sway when the experimental research on tokamak systems by Soviet scientist Lev Artsimovich showed that the tokamak was a more efficient concept.

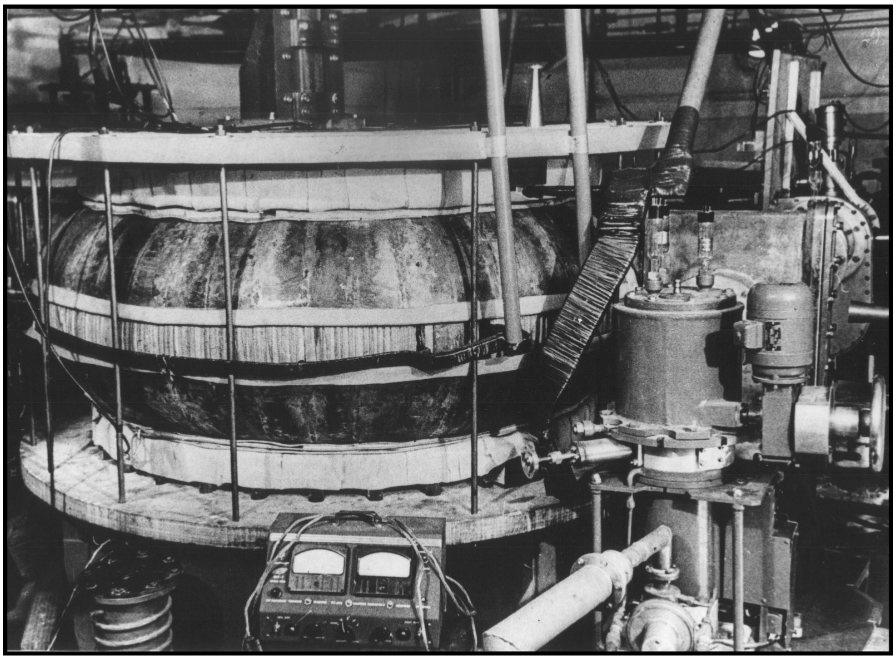

Figure 1.8: World's first tokamak device: Russian T1 tokamak

1970-1980: Designs on JET and beginnings for ITER

By the 1970s it was clear that attaining fusion energy would be one of science's greatest challenges and collaboration might be key to meeting the challenge. European countries came together and began design work on the Joint European Torus, JET, in 1973. In 1977, the European commission gave the green signal for the project and Culham in Oxford, UK, was selected as the site for JET. The construction of JET, which would become the largest operational magnetic confinement plasma physics experiment, was completed on time and on budget in 1983 and the first plasmas were achieved. Medium-sized tokamaks in the 1980s introduced the extensive use of auxiliary heating techniques. The addition of the divertor demonstrated improved confinement; wall conditioning techniques were also introduced. Larger tokamaks like JT-60 (Japan), TFTR (US), T-15 (Soviet Union)—were also built to study plasmas in conditions as close as possible to those of a fusion reactor and regularly upgraded based on advances in fusion science. New features such as superconducting coils, deuterium-tritium operation, and remote handling were introduced. The 80's also saw the iron curtain being lifted slightly when ITER was set in motion at the Geneva Superpower Summit in November 1985. The idea of a collaborative international project to develop fusion energy for peaceful purposes was proposed by General Secretary Gorbachev of the former Soviet Union to US President Reagan.

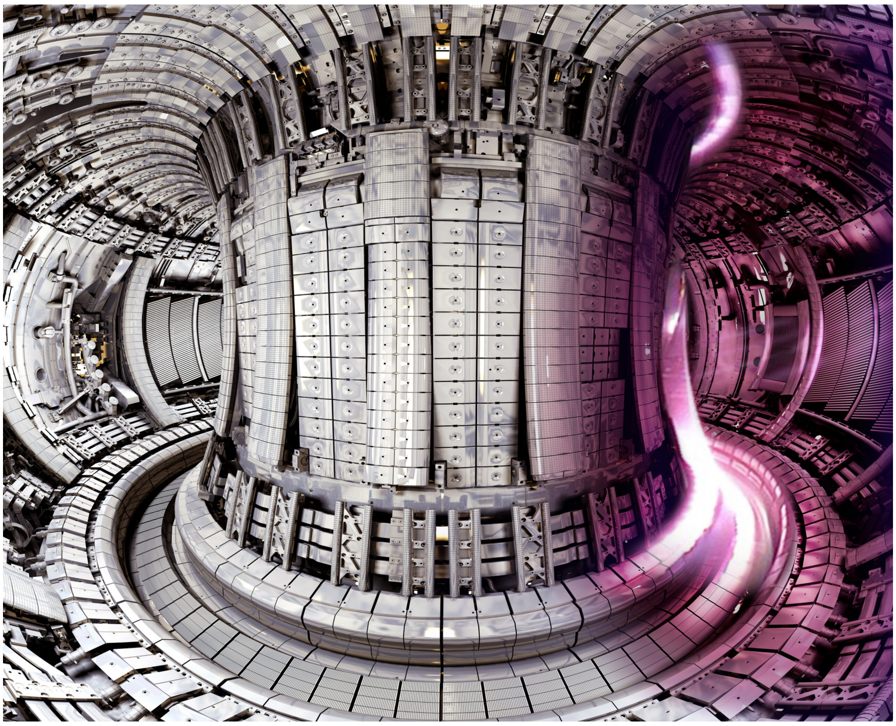

Figure 1.9: Interior of Joint European Torus JET

1980-2000s: JET record

The first experiments using tritium was carried out in JET, making it the first reactor in the world to run on the fuel of a 50-50 mix of tritium and deuterium. In 1997, using this fuel, JET set a world record for fusion output at 16 MW from an input of 24 MW of heating. This is also the world record for Q, at 0.67. It should be stated that the world record was achieved in a very short instant of about 1 second. A Q of 1 is breakeven, and to achieve fusion energy the Q value must be greater than 1. The aim of ITER is to achieve a Q of 10. Steady progress has been made in fusion devices around the world. The Tore Supra tokamak in France holds the record for the longest plasma duration time of any tokamak: 6 minutes and 30 seconds. The Japanese JT-60 achieved the highest value of fusion triple product—density, temperature, confinement time—of any device to date. US fusion installations have reached temperatures of several hundred million degrees Celsius.

2000-present: A home for ITER

In 2005, the ITER Members unanimously agreed that ITER would be built in Cadarache in France. In December 2022, the ITER project passed the 77.7% milestone of work scope completed to first plasma. In 2015 the Wendelstein 7-X stellarator, which is a long-term back up strategy for the tokamak in the European

Fusion Roadmap came into operation, and its first operational campaigns exceeded all expectations.

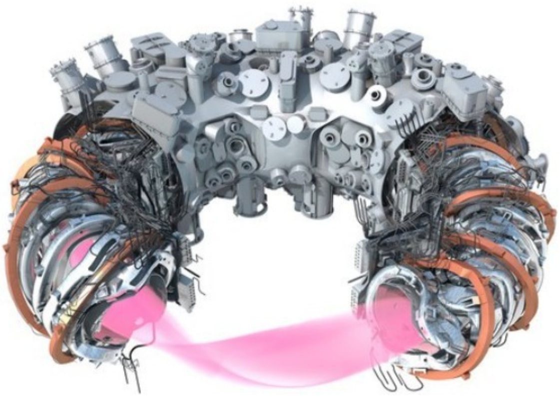

Figure 1.10: Wendelstein 7-X stellarator

In 2021 a new fusion energy world record of 59 MJ was achieved in JET in a 5 second long pulse, while burning only 170 micrograms of deuterium and tritium. Since the 1950s, more than 200 tokamak devices have contributed to the steady progression of research in magnetic confinement fusion. Today, veteran machines in China, Europe, India, Japan, Korea, Russia and the United States are re-orienting their scientific programs or modifying their technical characteristics to reinvent themselves—partially or totally—as test beds for ITER and for the next machine, DEMO.

Figure 1.11: Comparison of the plasma volumes

DEMO is the successor of the international fusion experiment ITER and the next step on the way to realise fusion energy. Its purpose is to develop and test technologies, physics regimes and control routines for operating a fusion reactor not as a scientific experiment, but as a power plant [1].

1.4 Engineering Challenges

Materials resistant to extreme conditions: The intense flux of high-energy neutrons and other particles generated during fusion reactions subject the reactor's structural materials to extreme conditions. Finding materials capable of withstanding these conditions while maintaining structural integrity is a top priority. These materials must be compatible both with the requirements of plasma purity, and also with the harsh thermal, radiation and vacuum environments inside the reactor.

Heat exhaust management in the divertor region: One of the primary challenges in fusion reactor design is managing the heat and particle exhaust from the plasma. In tokamaks like ITER, this is accomplished through a component called the divertor, which extracts heat and particles from the plasma and protects the reactor's walls from damage. The extreme power density conditions in the divertor region present significant engineering challenges.

Remote handling for maintenance: Fusion reactors operate in harsh environments that are inaccessible to human operators. As a result, maintenance and repair tasks must be performed remotely using advanced robotic systems. Reliable and efficient Remote handling technologies in a practical fusion reactor environment remains a significant engineering hurdle. Research efforts are focused on enhancing the dexterity, agility and autonomy of remote handling systems to enable efficient maintenance operations in future fusion power plants and to optimize the size of associated maintenance facilities.

Tritium fuel cycle: Tritium, a radioactive isotope of hydrogen, is a key fuel for deuterium-tritium (D-T) fusion reactors. However, tritium is not naturally abundant and must be produced artificially. Additionally, tritium has a relatively short (12.3 year) half-life. Developing efficient tritium breeding and extraction techniques is essential to sustaining fusion reactions in a practical D-T reactor.

Efficient heat removal for electricity generation: While fusion produces intense energy, the physical structure of tokamak fusion reactors is that of a geometric heat source, poorly configured to efficiently remove the heat produced from the fusion reaction. Traditional heat removal designs used in fossil fuel or nuclear fission plants interface directly with the heat generation process, whereas in a fusion reactor any such interface would disrupt the plasma and stop the fusion reaction [1].

1.5 Main components

superconducting magnet system: consists of three primary components: the Toroidal Field (TF) coils, the Poloidal Field (PF) coils, and the Central Solenoid (CS).

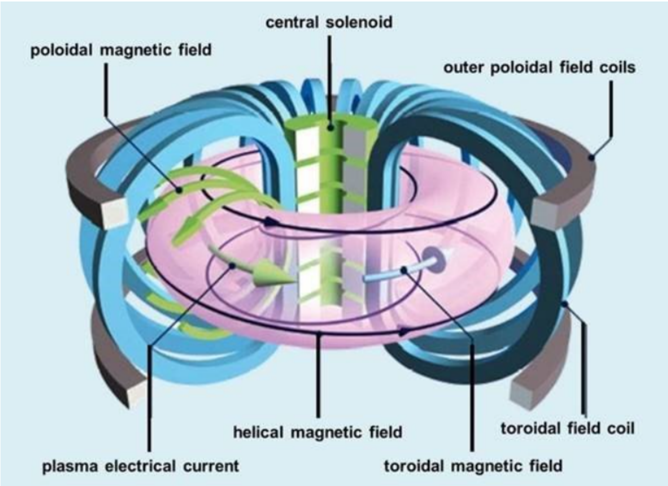

Figure 1.12: Schematic drawing of Tokamak superconducting magnet

Vacuum vessel: a hermetically sealed, double-walled steel container that creates the necessary high-vacuum environment for the fusion reactions and acts as a first safety containment barrier and provides support for in-vessel components such as the blanket and the divertor.

Figure 1.13: Vacuum vessel

Blanket: blanket modules completely cover the inner walls of the vacuum vessel protecting the steel structure and the superconducting toroidal field magnets from the heat and high-energy neutrons produced by the fusion reactions. Each module consists of a replaceable First Wall Panel, which directly faces the plasma, and a main Shield Block for structural support and neutron shielding. As the neutrons are slowed in the blanket, their kinetic energy is transformed into heat energy and collected by the water coolant. In a fusion power plant, this energy will be used for electrical power production.

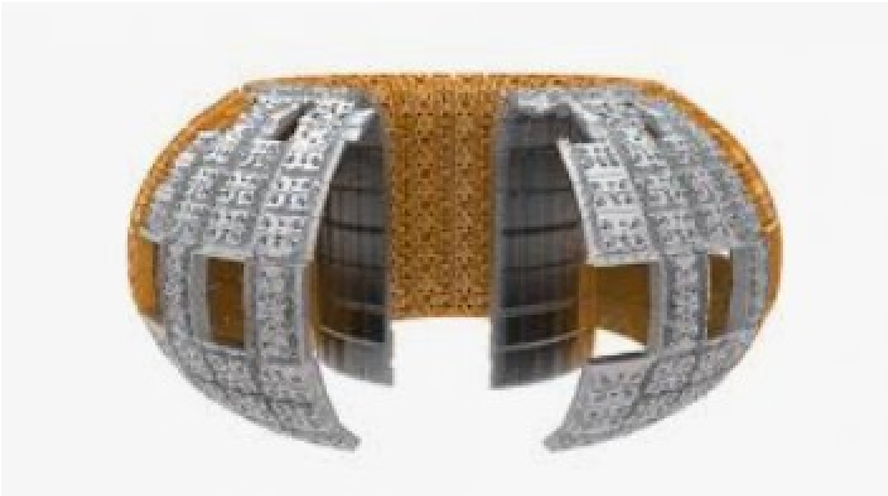

Figure 1.14: Blanket

Divertor: Situated at the bottom of the vacuum vessel, the divertor extracts heat and ash produced by the fusion reaction, minimizes plasma contamination, and protects the surrounding walls from thermal and neutronic loads.

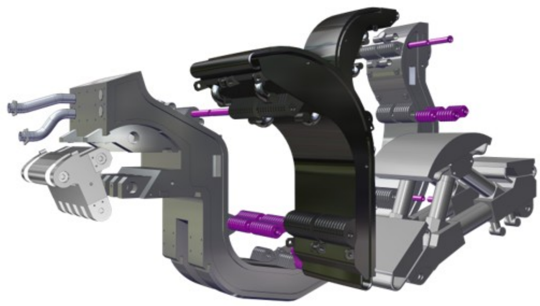

Figure 1.15: Divertor

Cryostat: A massive, outermost vacuum chamber made of stainless steel that encloses the entire reactor core, providing the essential high-vacuum insulation necessary to prevent heat transfer to the sensitive, cold components, ensuring an ultra-cool environment and also acting as a key part of the structural support system.

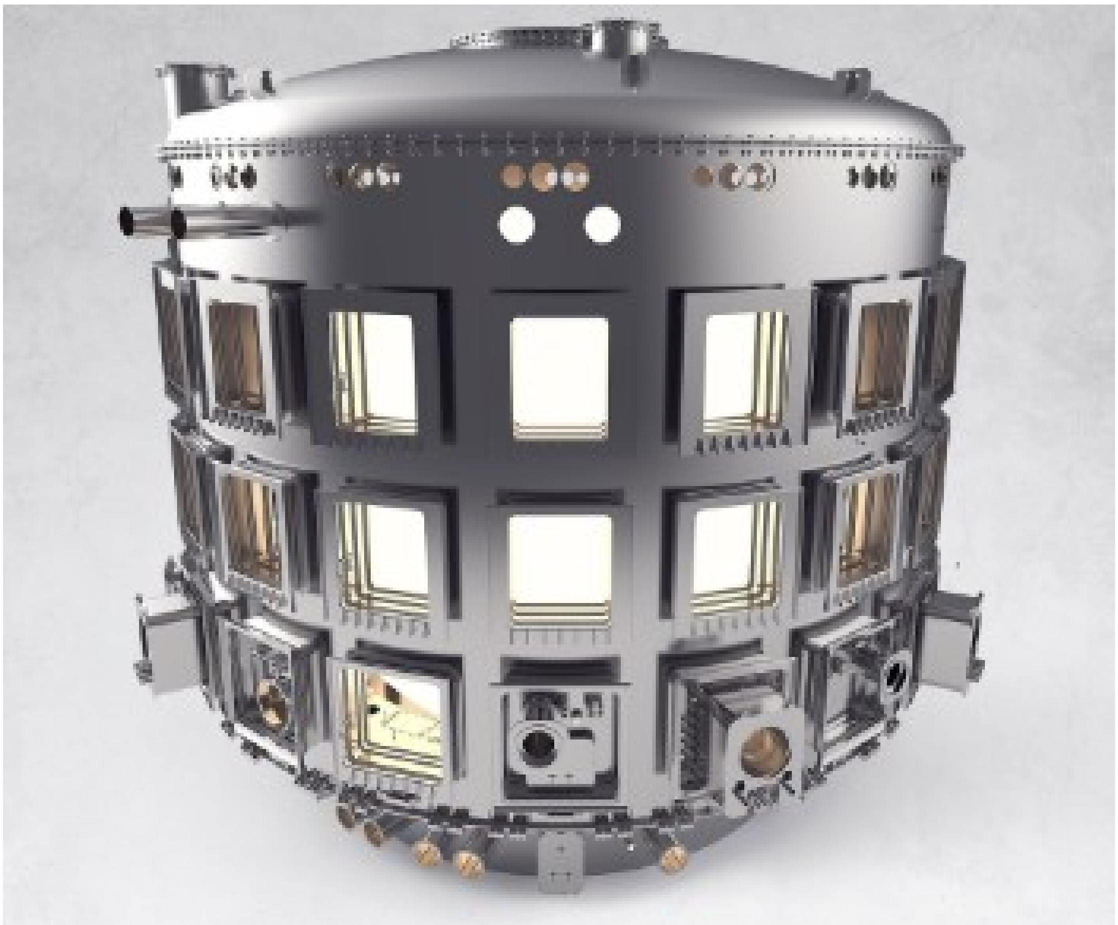

Figure 1.16: Cryostat

Thermal shield: a critical component devoted to minimising the heat loads from the tokamak warm components, to the superconducting coils operating at 4.5 K. It consists of stainless-steel panels that are either highly polished or coated with silver for low emissivity. They are actively cooled by helium gas flowing inside of a cooling tube welded to the panel surface; during plasma operation, the temperature of the helium gas ranges from 80 K to 100 K.

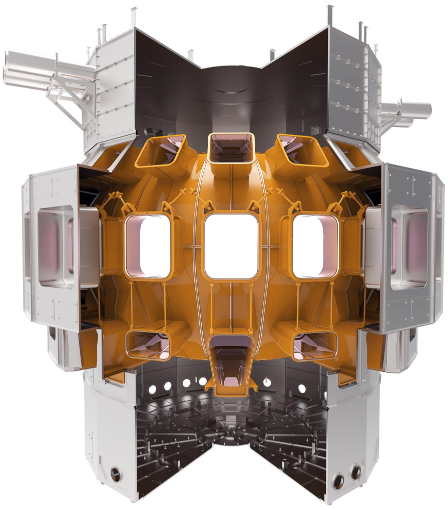

Figure 1.17: Thermal shield

1.6 DTT

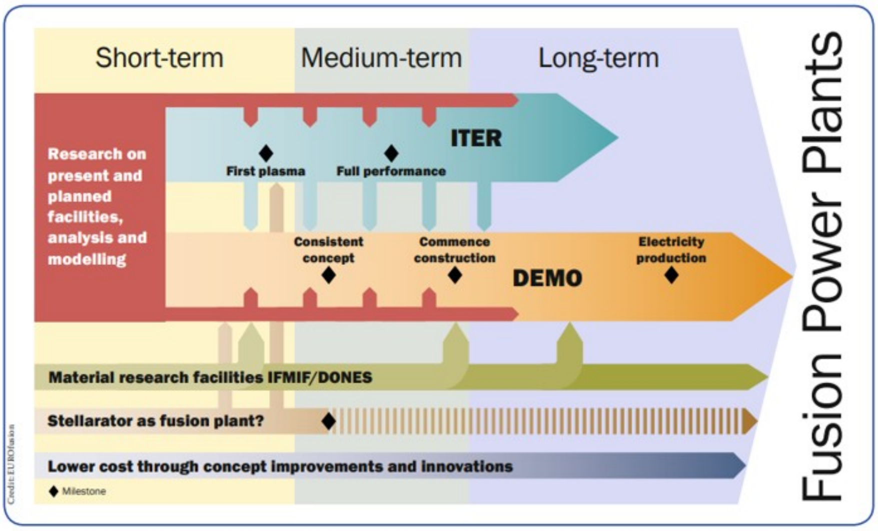

Figure 1.18: The European Roadmap in a nutshell

The Divertor Tokamak Test facility (DTT) is a new Italian fusion project that aims to address one of the major challenges identified in the European Fusion Roadmap: i.e., exhausting power from fusion reactors. In a reactor, most of the energy will flow out isotropically through neutrons, which will be absorbed by appropriate blankets around the machine. However, a significant amount of thermal power will be lost by the plasma as radiation, convection and conduction. The latter two, in particular, originate very high and localized heat loads on the device first wall, and in particular on the divertor, which is the system that collects the energy flowing out from the plasma through charged particles. The heat flux on the divertor can be very large, of the same order of the heat flux on the Sun! The divertor must withstand harsh conditions and is one of the most critical components of a fusion system.

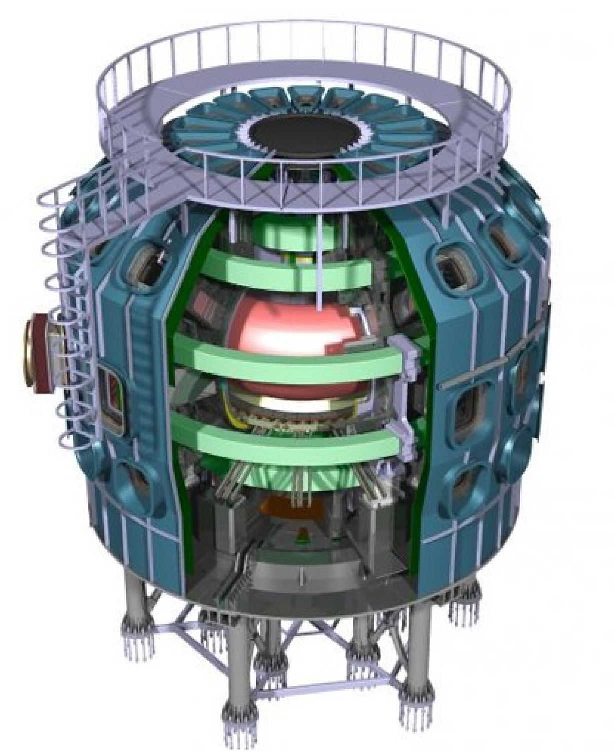

Figure 1.19: DTT

The urgency for a research effort on the plasma exhaust issue and on the divertor is now broadly recognized in the international community, and in particular in the European Fusion Roadmap, as one of the main challenges in view of the construction of a demonstration plant DEMO. DTT will begin operation with a tungsten-armoured divertor using the same technology developed for ITER. But it is also designed with the flexibility to try different divertor and magnetic geometries and, later, more esoteric approaches such as liquid metal targets that cannot be deployed on ITER. The project, first proposed in 2015, is led by the Italian national Agency for New Technologies, Energy and Sustainable Development (ENEA) in collaboration with the Italian fusion community and international institutions. The DTT facility will be located in the ENEA premises in Frascati[2].

1.7 DTT Thermal shield

The Thermal Heat Shield (THS) is a critical component of the DTT system, designed to minimise heat transfer between the Vacuum Vessel (VV) and the superconducting magnet system operating at 4.5 K. Thermal insulation is achieved through two primary mechanisms: the reflection of radiative heat loads and the reduction of conductive heat pathways at structural interfaces. Convective heat transfer is inherently eliminated by the cryostat, ensuring that the temperature-sensitive superconducting components are shielded from all principal modes of heat ingress.

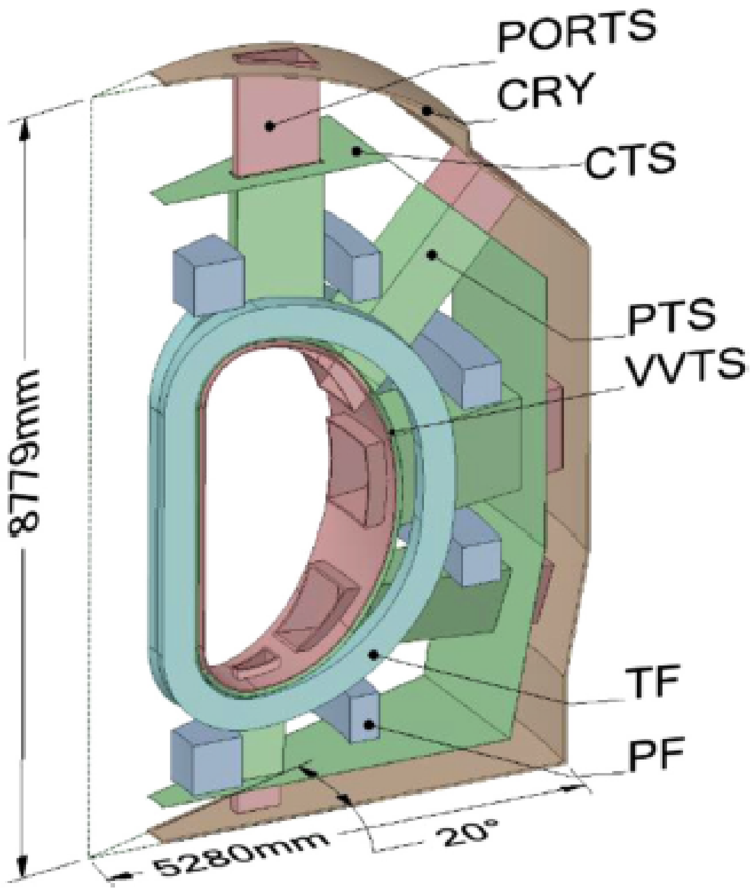

Figure 1.20: DTT thermal shield

The THS is subdivided into three main regions covering respectively the vacuum vessel (VVTS), the ports (PTS) and the cryostat (CTS). It is arranged, along the toroidal direction, in 18 electrically insulated segments (20 deg each), composed of several stainless-steel modules (AISI316L). Each module consists of a double sheet structure, joined together by lateral ribs (3mm thick) along the two edges in the poloidal direction enclosing the cooling tubes where the pressurized helium gas circulates (1.8MPa, 80-100K). A simpler, single-panel solution is envisaged as well. The cooling tubes are welded onto the innermost shell. More specifically, the TS cooling system consists of 36 independent lines (in parallel). The Vacuum Vessel (VV) is kept at a temperature between 60 and 70°C during the plasma operating state (POS), and 110°C during the baking phase (BAK). The VV temperature is controlled by means of the hot demineralised water that circulates through its double shell structure. Similarly, the Cryostat is maintained at room temperature (about 22°C) by means of specific heaters placed on its external surface [3].

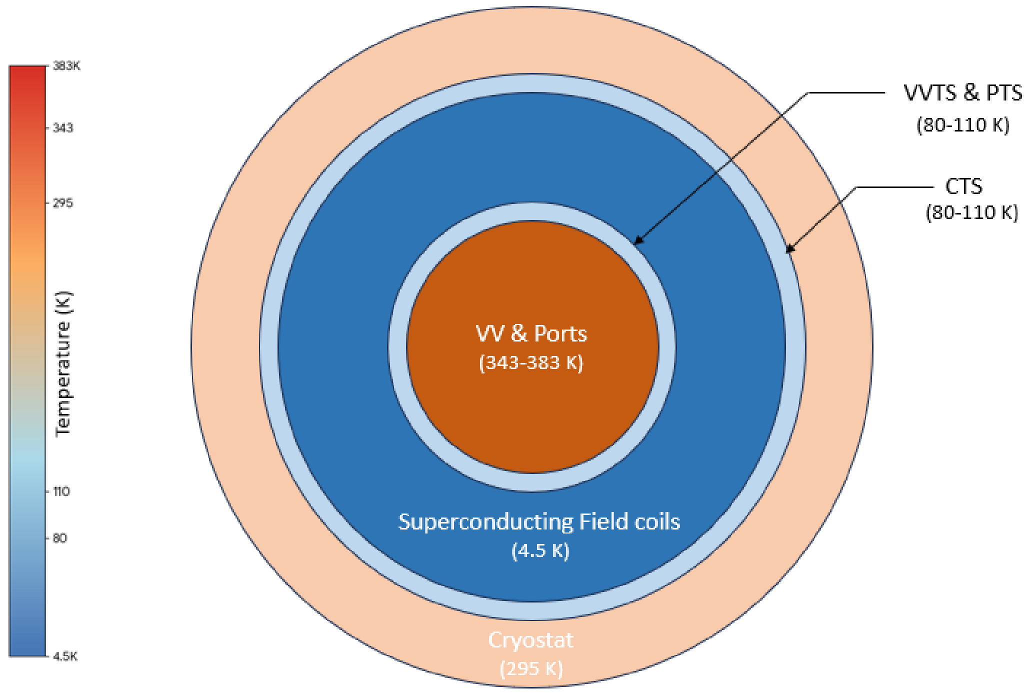

Figure 1.21: DTT Operating Temperature Zones

1.8 Scope & Objective

The Divertor Tokamak Test (DTT) facility is currently in its engineering design phase. Preliminary thermal analyses of its Thermal Shield (TS) system have already been completed. These initial studies, conducted using ANSYS Mechanical and RELAP5-3D, have successfully quantified the global radiative heat loads on the TS and superconducting magnets, assessed the effectiveness of Multi-Layer Insulation (MLI), and characterized the thermohydraulic performance of the helium cooling circuit. However, a comprehensive thermo-mechanical analysis is now required to ensure the structural integrity and operational reliability of the TS under the combined effects of thermal, mechanical, and electromagnetic loads. The current design, as detailed in involves complex support systems, introduces toroidal and poloidal cuts to mitigate eddy currents, and must accommodate significant thermal displacements between components operating at vastly different temperatures.

The work presented in this study is integral to the Port THS design process, providing critical insights into its thermo-structural behavior under operational conditions. By evaluating the displacement and stress fields resulting from thermal loads, this study aims to verify structural integrity and inform potential design optimizations. FEA is employed using ANSYS FE software to simulate realistic operating scenarios, incorporating temperature-dependent material properties for enhanced accuracy and reliability in performance predictions. The findings of this study contribute to ensuring the reliability and efficiency of the DTT THS, which supports the broader goals of the facility in advancing fusion technology. The specific objectives are:

- Develop a finite element (FE) model of the PTS–port assembly.
- Perform finite element analysis (FEA) to evaluate the structural stability of the assembly under steady-state thermal and gravitational loading.
- To identify and quantify critical regions of high stress, excessive deformation, or potential interference with adjacent components.
- Verify that relative gaps between the port duct, inner PTS, and outer PTS are maintained across all loading conditions. To optimize support locations to ensure that no local contact areas form due to thermal deformations.

Chapter 2

Literature review

2.1 State of the Art in Tokamak Thermal Shields

2.1.1 ITER thermal shield

ITER Thermal Shield (TS) assembly comprises the vacuum vessel (VVTS), cryostat (CTS), and support (STS) thermal shields. The TS utilizes single-wall structure primarily fabricated of stainless steel, covered on both sides with a thin, low emissivity layer of silver to keep the emissivity value below 0.05. It is actively cooled by helium gas flowing through surface-welded tubes [4].

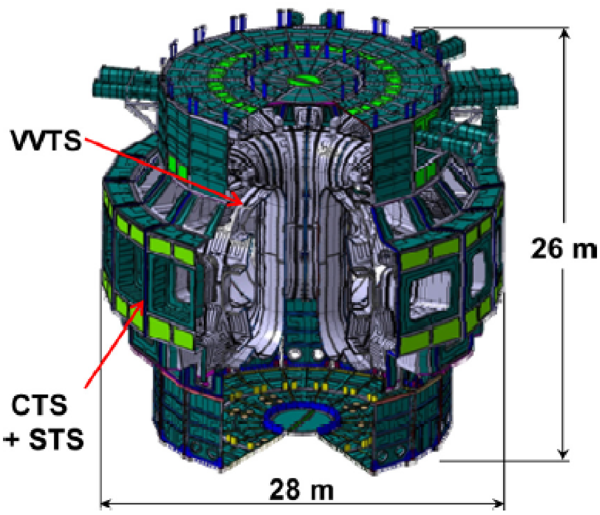

(a) VVTS and CTS/STS

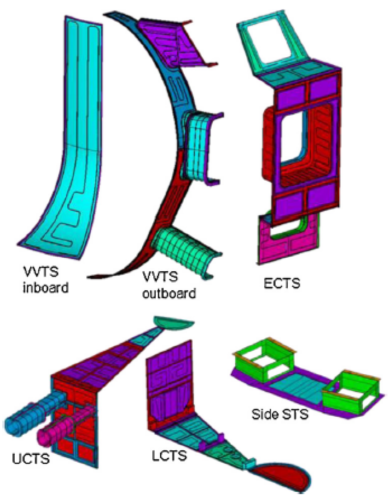

(b) Finite element models of representative TS sectors.

Figure 2.1: ITER Thermal shield

VVTS is made up of inboard and outboard 10° sections. It is self-standing structure supported from the toroidal field coil(TFC) cases at the upper level of the equatorial port. Each section consists of panels welded to flanges at the edges. Two parallel panels, 10 mm thick on the VV side and 5 mm thick on the TFC side, are used for both the outboard VVTS and the VVTS along ports. These panels are individually welded to the flanges with a nominal 10 mm spacing between them. The inboard section is made of single panels of 20 mm thick plate. The sections are connected with the help of bolted joints. The joint halves are bolted to the flange through insulation shims. These form 36 electrical breaks in the toroidal and two electrical breaks in the poloidal direction to considerably reduce induced electro-magnetic (EM) loads.

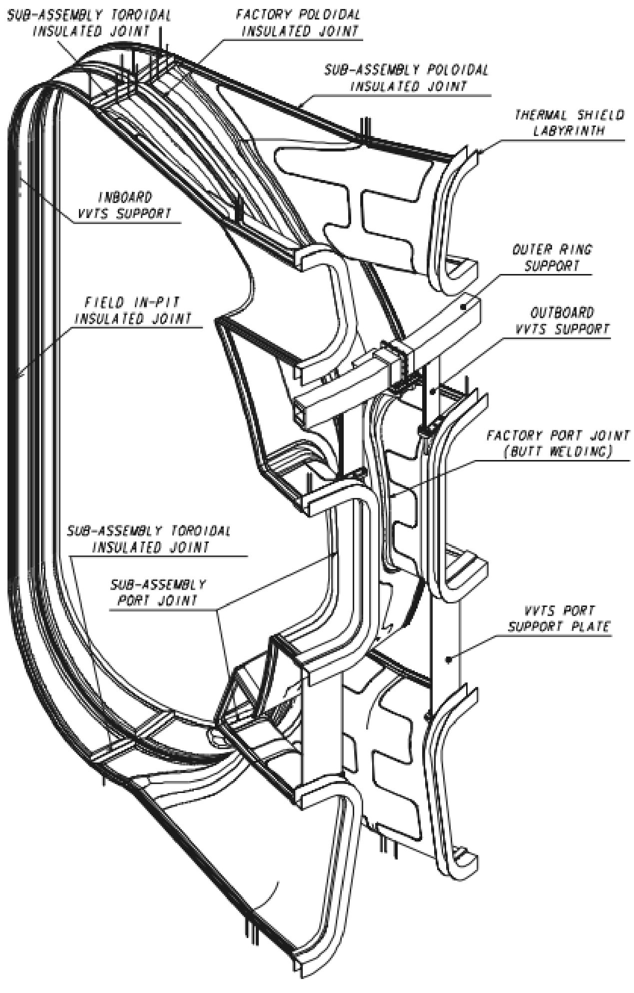

Figure 2.2: Vacuum vessel thermal shield 20° sector

CTS panel is made up of a 9 mm stainless steel plate reinforced at the corners and U-shaped ribs at the edges and at the center lines. Four titanium alloy supports provide fastening of the panel to warm components. Cooling tubes, bent in a serpentine manner, are welded to the panel from the cold side via 2.5 mm thick L brackets. The outlet of one panel and the inlet of the next one are connected by a flexible tube loop. Labyrinths at the edges interface between panels. This permits mutual thermal and seismic displacement, provides vacuum pumping gaps and prevents penetration of thermal radiation from warm components. The interfaces between VVTS, TTS, STS and CTS thermal shields are labyrinth structures also.

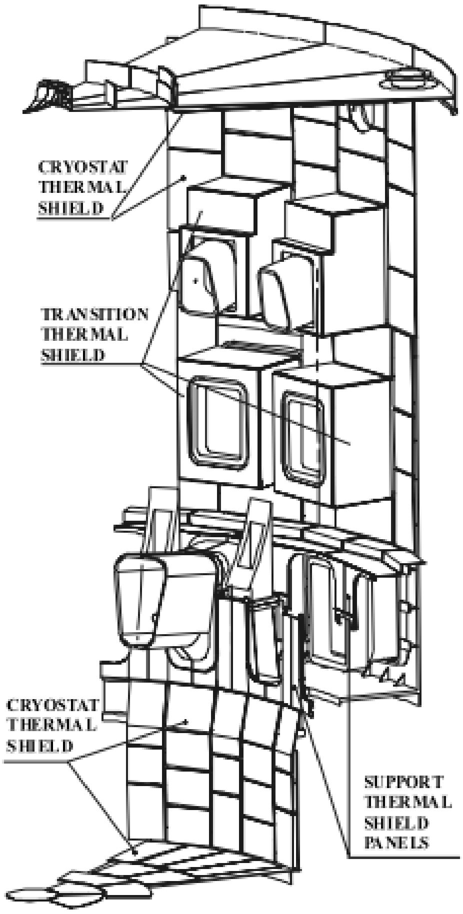

Figure 2.3: Cryostat, transition and support thermal shield panel layout.

Structural analysis Both Global and local analysis have been performed to verify structural stability for the ITER thermal shield. Global analysis focuses on the determination of displacement and primary stress intensity as well as reaction force in the inboard/outboard support. Local analysis intends to check stress level in the TS joint. The main loads on the TS are gravitational, seismic, electromagnetic forces and TF coil out-of plane deformation. Structural analysis was conducted for each load applied on the TS and load combinations were also considered to verify the new design.

The results show that maximum stress is within allowable limits. Maximum mutual displacement of joint flange is obtained for local joints models from post processing global results of load combination. The global flange displacements become boundary conditions for local joints model in sub-modeling approach. The inboard side of the VVTS is inaccessible after machine assembly and the access to the other thermal shields is difficult. Thus, a very high reliability throughout the lifetime of the ITER machine with large spectra of loading conditions is required. The main loads on the thermal shield are gravity, seismic, electromagnetic and thermal gradients. The VVTS has, in addition, contact loads and displacements imposed by the TF coil deformation.

Thermal analysis The layout of the cooling tube tracing is important in order to satisfy the heat load criteria for the TS. The cooling tube is to be welded on the TS surface in zigzag pattern, hence, the distance between the adjacent tubes is one of the major parameters for the TS design. The maximum cooling tube distance for each part of TS is determined by satisfying the overall heat load design condition. For thermal analysis three major simplifications were made in the models: cooling tube welding geometry, cooling tube connection and support of CTS.

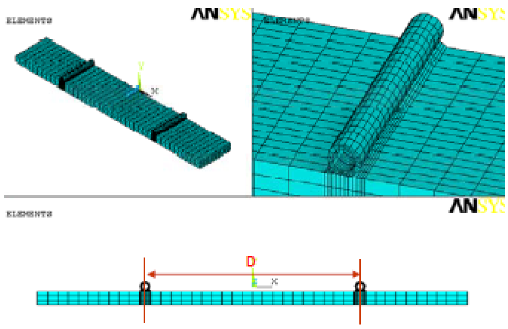

Figure 2.4: Simplified FE model for thermal anslysis.

The operating pressure in the cooling tube is 1.8 MPa. The inlet and outlet temperatures of the cooling tube for each segment are 80 K and 100 K under plasma operating condition. The temperatures of vacuum vessel, cryostat and magnet are 393 K, 300 K and 4.5 K, respectively. The boundary conditions applied are the radiant heat loads to the TS, the heat flux to the TS associated with the support, and heat transfer coefficient between helium and the cooling tube surface. The cooling tube distance is obtained for different parts of the thermal shield from the analysis results from 3D simple model [5].

2.1.2 JT-60SA thermal shield

The JT-60SA thermal shield adopts a fundamentally different structural approach: a double wall structure made of 316 L stainless steel (Co<0.05 wt %) with helium cooling pipes integrated within the wall cavity. The TS consists of the vacuum vessel thermal shield (VVTS), the cryostat thermal shield (CTS) and the port thermal shield (PTS) as shown in Fig. 2.4(b). The superconducting coils consist of 18 toroidal field coils (TF), a central solenoid with 4 modules (CS), 6 equilibrium field coils (EF). TS is divided into 18 segments electrically insulated from each other to prevent excessive electromagnetic forces during disruptions. Twenty degrees and forty degrees sectors of the VVTS are pre-assembled in the factory during the coupler customization. The vacuum vessel (VVTS) and port (PTS) thermal shields consist of two panels reinforced by edge frames and gaseous (80K) He cooling pipes, fitting snugly in the gap between TF coil and vessel. The cryostat thermal shield (CTS) is single-walled with multilayer superinsulation.

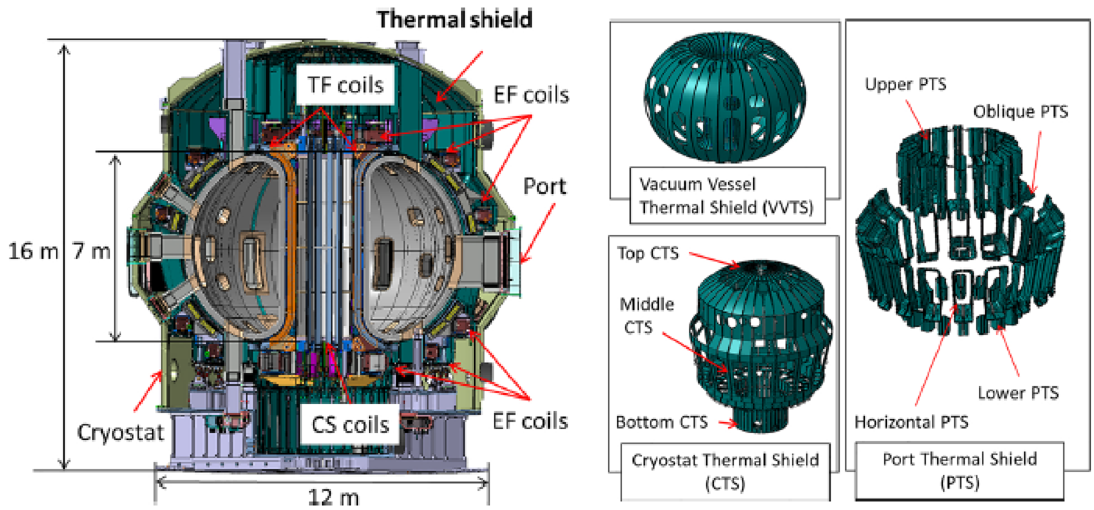

(a) Section view of JT-60SA. **(b)** Thermal shield.

Figure 2.5: JT-60SA Thermal shield

Structural analysis was performed by a simplified 360-degree model built up by arranging identical 20-degree sector models. In analysis, the cooling pipes inside the thermal shield are neglected for simplicity. The thermal shield weight without pipes is adjusted by increasing the material density (SUS316L density: 7980 kg/m3, Increased SUS316L density: 11474 kg/m3)[6].

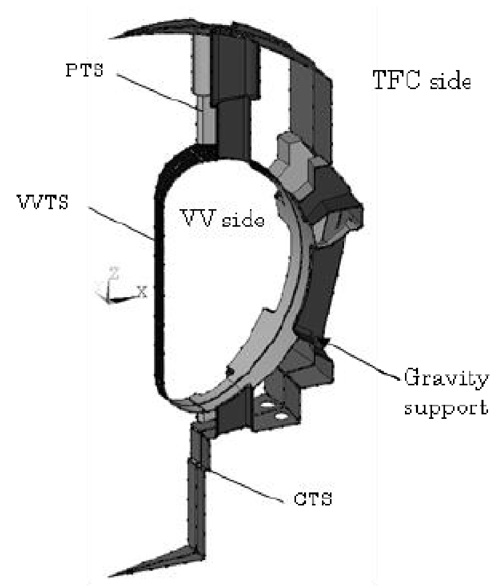

Figure 2.6: Analysis model of the thermal shield for 20 degree

The analysis considers two distinct operational states: the assembly condition and the cooldown condition. In both cases, a gravitational acceleration of 1.0 G is applied. The temperature assigned to the assembly condition is 300 K, representing the ambient room temperature state at which the thermal shield is installed and mechanically connected to the surrounding structure. The cooldown condition is assigned to a temperature of 80 K, corresponding to the nominal operating temperature of the actively helium-cooled thermal shield during machine operation.

The thermal shield gravity support adopts a link structure at both ends of the shaft located at the centre of the cylinder. This configuration is specifically designed to provide a degree of freedom in the horizontal direction, allowing the thermal shield to accommodate the relative thermal displacements that occur during cooldown between the shield structure and the adjacent components, without generating excessive constraint forces at the support interfaces. A static seismic analysis of the thermal shield was performed separately by a simplified 360-degree model built up by arranging identical 180-degree sector model to estimate forces loaded to joints of the thermal shield.

Therml analysis of the VVTS and the PTS was performed by a two dimensional model in order to determine the layout conditions of cooling pipes in the VVTS and the PTS. Analysis was performed with distance (L1) between the rib and the cooling pipes of 0 mm, 40 mm and 60 mm. For distance between the cooling pipes (L2), 300 mm and 400 mm are taken (see Fig. 2.6). For all the layout conditions above, same 80 K helium flow rate of 7.44 g/s is used. SUS316L emissivity of the ambient and cryogenic components side and inside the thermal shield is assumed to be 0.15 and 0.30, respectively. The thermal shields receive a radiation heat from the 323 K ambient component and emit it to 4.4 K cryogenic components.

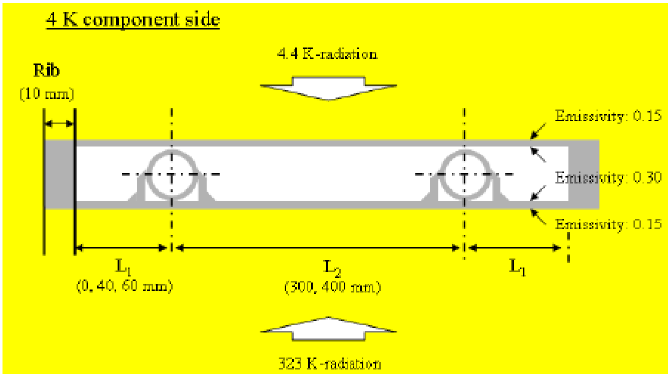

Figure 2.7: Layout condition of the cooling pipes inside the VVTS and the PTS

Thermal analysis results determined the distance limit between the pipe and the rib of 400 mm, and the pipe pitch limit of 300 mm. When these conditions are difficult to be satisfy, either the distance between pipe and rib or the pipe pitch can be decreased to 60 mm or 400 mm, respectively.

Thermal analysis of the CTS is performed by a two dimensional models in order to determine the layout condition of cooling pipes inside the CTS.

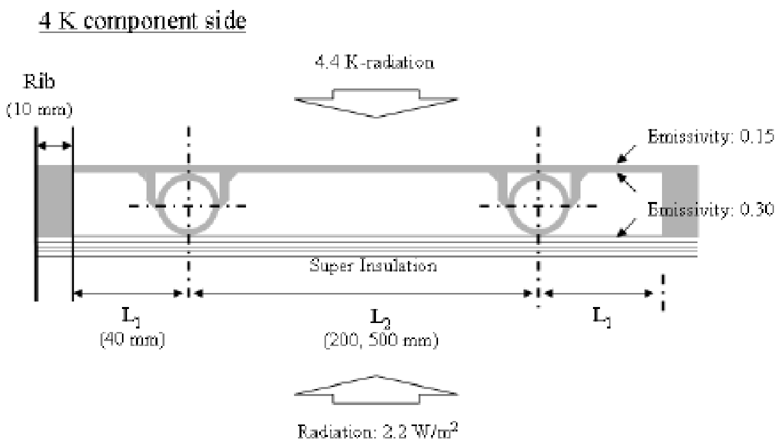

Figure 2.8: Layout condition of the cooling pipes inside the CTS

Thermal analysis results determined the distance limit between the pipe and the rib of 40 mm, and the pipe pitch limit of 1000 mm [7].

2.2 Design Requirements of DTT THS

Thermal

- Reduce the radiative heat flux to the magnets below q”mag = 1 W/m2.
- Minimize heat load to the cryoplant (Tin = 80 K).
- Actively cool the thermal shield with redundancy to maximize availability.
- Reduce the hydraulic impedance ($<$ 2 bar) $\rightarrow$ flexibility in the refrigerator design/operation.

Mechanical

- Withstand static (e.g. dead weight) and dynamic (e.g. electromagnetic, seismic) loads.
- Minimize electro-magnetic loads (eddy currents).
- Maintain relative displacement between the VV, the coils, the ports, the TS, and the cryostat are caused by out-of plane deformations.

Integration

- Comply to the assembly sequence.
- Reduce space occupation (no interference with other subsystems) [8].

2.3 Current Status of the DTT Thermal Shield Design and Analysis

The DTT thermal shield follows the JT-60SA design approach, adopting a double-wall panel construction with active helium cooling for the vacuum vessel and port thermal shields, and a single-wall panel with active helium cooling and Multi-Layer Insulation (MLI) for the cryostat thermal shield, in contrast to the ITER approach of single-wall actively cooled panels with silver electroplated surfaces ($\varepsilon \leq 0.05$), reflecting both the intermediate scale of the machine and the manufacturing maturity demonstrated by the JT-60SA. Cooling pipes are welded to the panel surface using a staggered welding sequence, consistent with the approach employed in the ITER thermal shield.

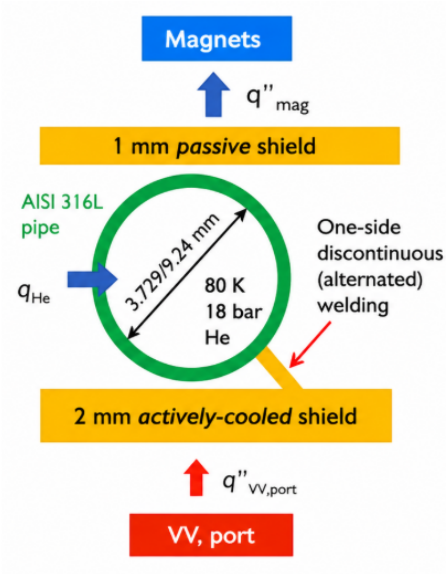

(a) Cross-sectional layouts of VVTS/PTS.

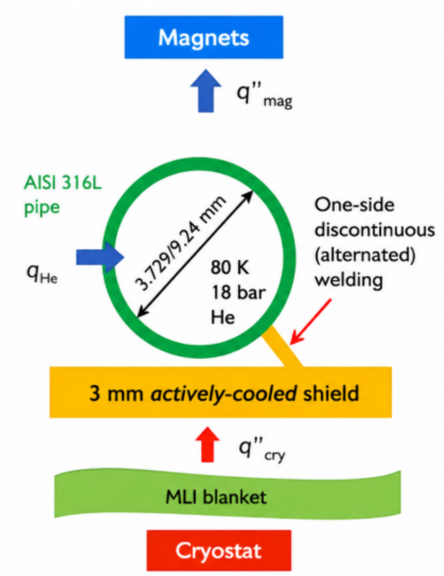

(b) Cross-sectional layouts of CTS.

Figure 2.9: DTT thermal shield [8].

To minimize radiative heat transfer without the complexity of silver plating, specific mechanical finishing standards are applied to the thermal shield surfaces. The emissivity (ϵ) is controlled primarily through precision mechanical polishing to reduce surface roughness (R_a), as detailed below [8]:

Table 2.1: Surface finish and emissivity requirements of DTT THS at 80 K

Component	**Finish Standard**	**Roughness R_a [μm]**	**Emissivity ϵ at 80 K**
CTS	ISO N6	≤ 0.80	≤ 0.17
VVTS / PTS	ISO N4	≤ 0.20	≤ 0.07

The VVTS, PTS, and CTS are gravity-supported on the vacuum vessel (VV), the ports, and the cryostat, respectively, using electrically isolated bolts equipped with slotted holes to accommodate thermal contraction. The VVTS, PTS, and CTS are electrically and mechanically isolated from one another, with no direct contact between them, in order to minimize the formation of eddy currents.

Several thermal analyses of the DTT thermal shield have been conducted, yielding significant insights into the overall thermal behaviour of the system. Studies on the optimisation of cooling pipe layouts and hydraulic connections are currently ongoing, with the aim of refining the thermal performance ahead of the detailed design finalisation. Previous works on the thermomechanical analysis of the DTT Vacuum Vessel Thermal Shield provides a fundamental methodological reference for the present thermomechanical analysis of the DTT Port Thermal Shield, establishing the modelling strategy, load case definitions, and structural assessment criteria adopted in this thesis.

2.4 Thermo-mechanical analysis of DTT Vacuum Vessel Thermal Shield

The VVTHS is segmented into 18 electrically insulated toroidal sectors, each spanning 20 ◦ , with multiple cooling modules. Structurally, each 20 ◦ sector of the DTT Vacuum Vessel VVTHS, in turn divided into five non-continuous panels in the poloidal direction (two at the inboard, three at the outboard), is composed of two shells. These are referred to as the inner THS and outer THS, and they are connected to the VV through a bolt system that constrains relative displacements while allowing controlled thermal expansion. The CPs, integrated with the inner VVTHS, are welded along its surface and feature bellows at the gaps between adjacent panels, ensuring free thermal contraction of the THS system. The thicknesses of the VV, inner THS, and outer THS are 15 mm, 2 mm, and 1 mm, respectively. The internal and external diameters of CPs are 9.24 mm and 13.72 mm respectively, while the bolt diameter is 12 mm [9].

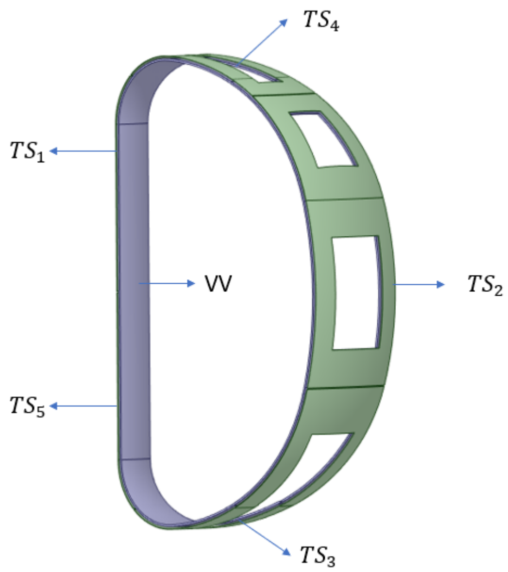

Figure 2.10: VVTS panels

2.4.1 Major Simplifications

- Thermal equilibrium is assumed across all components, with uniform and homogeneous temperature distributions applied to the VV and THS. Transient effects associated with reaching the target temperatures are neglected, and temperature-dependent mechanical material properties are incorporated. This simplification is considered appropriate at the conceptual design stage, where the focus is on the global structural response under thermal loading rather than the transient thermal history.

- For G10-CR temperature-dependent properties are used, with interpolation applied where data are unavailable. Due to the simplified stress-strain tensor resulting from the beam element formulation, only the lengthwise elastic modulus, crosswise Poisson's ratio, lengthwise thermal expansion coefficient, and lengthwise thermal conductivity are retained, with the remaining orthotropic properties neglected.

- The cooling pipes and bolts are modelled using beam elements, a simplification adopted to capture the overall structural behaviour and inter-component load transfer of the assembly rather than to resolve the detailed local stress state of these individual components [9].

2.4.2 FE model

The thermo-mechanical behavior of the THS is analyzed through FE simulations conducted using the ANSYS software. A simplified 360° global model is constructed by the periodic arrangement of identical 20° sector models, with cyclic symmetry boundary conditions applied at the toroidal cut planes. Due to thin thicknesses, both VV and THS were modeled using linear shell elements (SHELL181), while linear beam elements for both bolts and CPs were considered (BEAM188). The VV, THS, and CPs are constructed from SS 316LN. Conversely, the bolts are made of G10-CR, a material chosen for its ability to prevent electrical currents from flowing between the VV and the remaining components.

Mechanical scheme of bolt connections

The VV and THS are coupled by the presence of several bolts referred as fixed, hinged and non-hinged. Fixed bolts do not allow relative displacement and directly anchor the THS onto VV, meanwhile hinged bolts allow either relative poloidal or toroidal displacement, and non-hinged bolts permit both poloidal and toroidal relative displacement. All bolts are fixed to the VV and prevent local relative displacement of the THS shells along their own axis while allowing free rotation around the same axis.

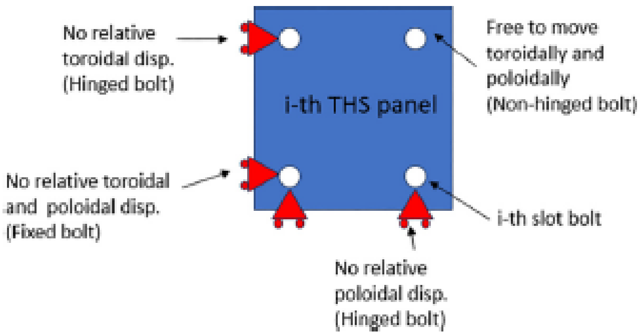

Figure 2.11: Mechanical scheme of bolt connections

Cooling pipes layout & Hydraulic connections

Two CPs flow along the inboard and outboard sides of the inner THS, effectively cooling it and preventing excessive heat flux from reaching the superconducting magnet system. To allow thermal contractions without inducing peak stresses and flexural effects on THS, between each panel bellows have been introduced. The extension of the bellows is along the toroidal direction, and their length was changed to understand their influence on the behavior of the whole assembly during the application of thermal loads.

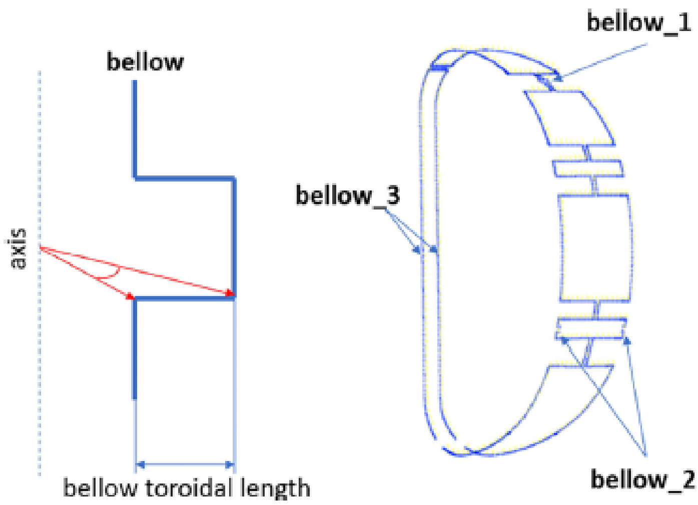

Figure 2.12: Representation of Cooling Pipes (CPs) and bellows

Results & Conclusions

Main objective of this analysis is to assess the deformation of the VV and THS under thermal loads, considering the presence of the CPs while varying the bellow lengths and evaluating the relative distances (gaps) between VV, inner THS and outer THS under different thermal loading scenarios. The main results of the analysis are as follows:

- The toroidal length of the bellows has minimal impact on the displacement and stress distributions of the VV, inner THS, outer THS, CPs and bolts.
- Relative gaps between the VV, inner THS, and outer THS were largely maintained, with only minor variations. The analysis confirmed that no contact occurs between the shells under the imposed thermal loads, preserving the system's operability.
- Although the displacement and stress distributions remained consistent across all scenarios, the analyses identified the bolts and CPs as critical components due to their significant stress levels. Therefore, it is necessary to employ more detailed models to capture the real stress condition acting on these components.
- Future research should focus on optimizing the number, location, and dimensions of the bolts to allow for controlled contraction and expansion of the components, thereby reducing localized stress concentrations.
- Additionally, the assumption of uniform component temperatures should be refined by including thermal gradients resulting from heat transfer through the cooling pipes. This enhanced modeling approach could provide a deeper understanding of thermo-mechanical behavior and support the further optimization of the DTT system [9].

Chapter 3

Methodology & Finite Element Modelling

3.1 Modelling Strategy and Analysis Workflow

This thesis will follow a systematic numerical analysis workflow, leveraging the foundational work from the provided research and expanding it into the mechanical domain. The process is outlined below:

Phase 1: Model Development and Definition of Load Cases

- Geometry and Mesh: THS CAD models without cooling pipes and welds, as developed in the DTT project will be used. A simplified 360° global model is constructed by the periodic arrangement of identical 20° sector models, with cyclic symmetry boundary conditions applied at the toroidal cut planes. A finite element mesh, building upon the preliminary ANSYS meshing strategies from preliminary analysis.

- Material Properties: AISI 316L stainless steel is assigned to the VV and thermal shield, and G10-CR glass-fibre reinforced epoxy composite to the bolt connections, the latter with temperature-dependent properties and interpolation where data are unavailable.

- FE model: The PTS is mechanically coupled to the port structure by means of several bolt connections, categorised as fixed, hinged, and non-hinged types. The bolts are represented using beam elements, while the ports, vacuum vessel and THS are modelled using shell elements. A detailed description of the bolt connection scheme and the port section cuts is provided in the subsequent chapters. Bolt connections are modeled using Bonded and No Separation contact formulations to ensure structural continuity and computational efficiency.

- Boundary Conditions and Load Cases: Steady-state thermal conditions are assumed, with uniform and homogeneous temperature distributions prescribed on the VV and thermal shield components. A gravitational body load of 9.81 m/s^2 is applied to the full model. Structural support is provided at Port 5, represented by a simply supported boundary condition that constrains all translational degrees of freedom at the support interface while permitting free rotation.

Phase 2: Finite Element Analysis (FEA)

- Contacts analysis: To verify the stability of the model, contact analysis is performed using the contact tool to evaluate the initial status, ensuring all interfaces are properly closed and the integrity of the load path is maintained before final execution

- Solver Setup and Solution: Utilizing the ANSYS Mechanical solver, static structural simulations are performed to determine the displacement, stress, and strain fields within the THS assembly. Structural analysis will be conducted for each load applied and load combinations.

- Post processing: Systematic extraction and interpretation of field variables to assess the structural integrity of the PTS assembly. Using post-processing tools, the results are visualized through contour plots.

Phase 3: Results Evaluation and Design Guidance

The results will be evaluated against the allowable criteria for AISI 316L and G10-CR to assess structural integrity. Key outputs for evaluation are total displacements and equivalent von Mises stresses, which help identify regions of high mechanical demand and verify that overall deformations remain within design tolerances. Contact analysis tools are employed to measure relative displacement between ports and PTS, while beam analysis tools are used to evaluate stresses and bending behavior in the bolts. Based on the findings, specific design recommendations will be formulated. This may include:

- Optimization of ports segmentation, number of bolts and its locations to maintain relative gaps between the ports, inner PTS, and outer PTS.

- Suggestions for modifying support flexibility to better accommodate thermal expansion.

- Assessment of the proposed use of a G10 sheet beneath the outer WTS plate to decouple eddy currents.

Phase 4: Validation and Reporting

The integrity of the finite element model and the accuracy of the results will be evaluated through analytical validation. Where applicable, simplified calculations—such as beam theory for support structures and fundamental thermal stress relations will be carried out to verify the order of magnitude and overall trends of the FEA results, ensuring that the model behaves consistently with first-principles expectations.

3.2 Geometry

A simplified 360° global model was developed by periodically replicating identical 20° sector models, with cyclic symmetry boundary conditions imposed at the toroidal cut planes. In the assembly, the ports were merged with the vacuum vessel to ensure structural continuity, while the port thermal shields (PTS) were connected to the ports by means of G10 gravity bolts. Wall thicknesses were assigned to each shell component according to their respective design values, as summarised in Table 4.1. The structural discretization relies on specialized element formulations to accurately capture the structural response while optimizing computational efficiency. The thin-walled configurations of the ports and port thermal shields (PTS) are modeled using SHELL181 elements, which are 4-node components featuring six degrees of freedom at each node[10]. This element formulation is well-suited for analyzing thin to moderately thick shell structures, as it incorporates first-order shear-deformation theory (Mindlin-Reissner shell theory) and accounts for finite membrane strains and large rotations. Conversely, the slender G10 gravity bolts are discretized using BEAM188 elements [10]. This 2-node, linear Timoshenko beam element includes shear-deformation effects and supports unrestricted axial, bending, and torsional loading modes. The combination of these two formulations ensures an exact mathematical representation of the structural coupling between the continuous shell surfaces and the discrete, slender bolt . For systematic identification, the port ducts are classified and numbered sequentially from top to bottom, spanning Port 1 through Port 5.

Table 3.1: Shell element thickness assignments.

Component	**Thickness [mm]**
Vacuum vessel & ports	15
PTS inner	2
PTS outer	1

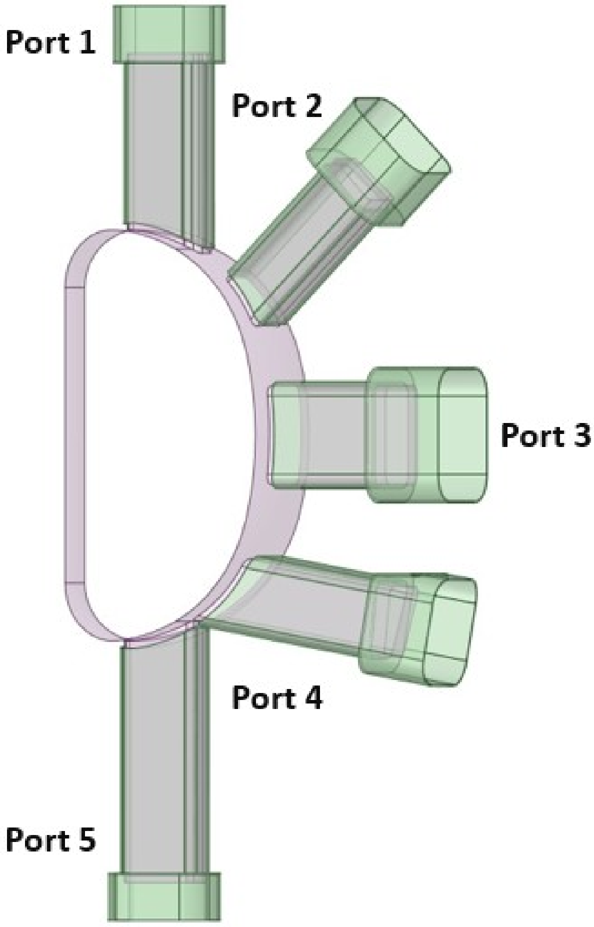

Figure 3.1: 20° sector geometry model in ANSYS spaceclaim

Bolt modelling

Each individual gravity bolt was represented by a pair of beam elements sharing a common centre node, as illustrated in Figure 4.2. This two-element configuration was adopted to provide an intermediate node at the mid-span of the bolt, which serves as the attachment point to the PTS inner shell. The two end nodes of the bolt beam, located at the extremities of the element pair, were connected to the corresponding attachment points on the shell surfaces of the adjacent structural components.

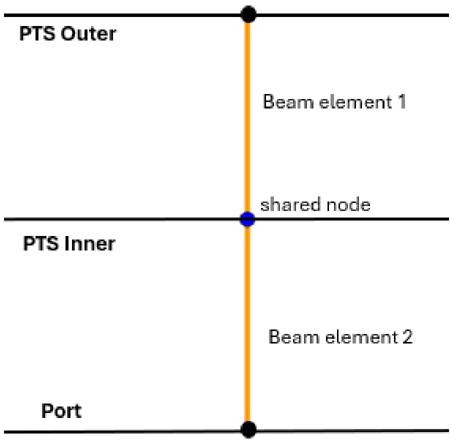

Figure 3.2: Bolt representation by a pair of beam elements with shared node

Beam-to-Shell Connectivity

At the beam nodes, contact definitions were employed to couple the beam nodes directly to the shell surfaces of the port and PTS. For the hinged bolt configuration, joint connections were additionally formulated between the beam element nodes and the shell surfaces, providing the kinematic constraints appropriate to the hinged behaviour described in Section 4.3. In order to provide geometrically consistent and uniquely defined attachment locations on the shell surfaces, vertices were created on the relevant shell faces by projecting pairs of intersecting lines onto the surface geometry. The resulting intersection vertices served as the reference points for the joint's definitions, ensuring that the bolt loads are transferred to well-defined nodes on the shell mesh rather than to arbitrary element faces.

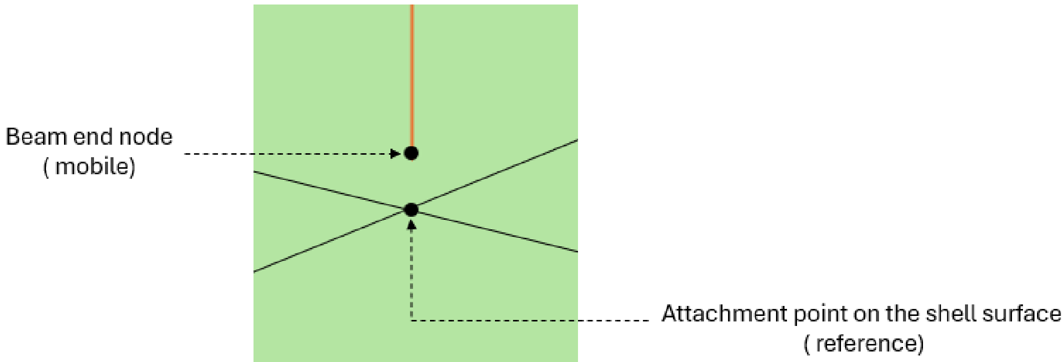

Figure 3.3: joint connections

3.3 Material properties

Two materials were assigned in the finite element model, reflecting the actual construction of the components: Stainless Steel 316LN for the vacuum vessel, ports and port thermal shields (PTS), and G10-CR fiberglass epoxy for the gravity bolts.

3.3.1 Stainless Steel 316LN

Stainless Steel 316LN was assigned to both the port and PTS shell elements. This austenitic stainless steel is widely adopted in cryogenic and nuclear fusion applications owing to its favourable combination of structural strength, toughness at low temperatures, and low magnetic permeability. Its mechanical properties are temperature-dependent and were defined in the model at four reference temperatures: 23°C, −193°C, 60°C, and 200°C, with 23°C taken as the reference temperature for thermal strain calculations.

Table 3.2: Stainless Steel 316LN mechanical and physical properties at reference temperature $T_{\text{ref}} = 23\,°\text{C}$.

Property	**Symbol**	**Value**
Density	$\rho\,[\text{kg/m}^3]$	8000
Young's modulus	$E\,[\text{GPa}]$	195 – 205
Poisson's ratio	$\nu\,[\text{-}]$	0.27 – 0.3
Yield strength	$\sigma_y\,[\text{MPa}]$	280 – 300
Ultimate tensile strength	$\sigma_{\text{UTS}}\,[\text{MPa}]$	580 – 780
Thermal expansion coefficient	$\alpha\,[\mu\text{m}/(\text{m}\,°\text{C})]$	16.5 – 17.5
Thermal conductivity	$\lambda\,[\text{W}/(\text{m}\,°\text{C})]$	14.4 – 15.6

Table 3.3: Stainless Steel 316LN temperature-dependent properties.

T [°C]	$\boldsymbol{\alpha}\,[\mu\mathbf{m}/(\mathbf{m}\,°\mathbf{C})]$	$\boldsymbol{E}\,[\mathbf{GPa}]$	$\boldsymbol{\lambda}\,[\mathbf{W}/(\mathbf{m}\,°\mathbf{C})]$	$\boldsymbol{\nu}\,[\text{-}]$	$\boldsymbol{\rho}\,[\mathbf{kg/m}^3]$
−193	~13.3	~210	~9.2		
+60	~16.3	~193	~15.0	~0.3	~8000
+200	~16.8	~183	~17.0		

Material references: Stainless steel, austenitic, AISI 316LN, annealed — ANSYS; ITER Appendix A, Material Design Limit Data.

3.3.2 G10-CR Fiberglass Epoxy

The G10-CR fiberglass epoxy composite was assigned to the gravity bolt beam elements. This material is commonly employed in cryogenic structural applications due to its low thermal conductivity, which minimises parasitic heat loads, combined with adequate mechanical stiffness. G10-CR exhibits orthotropic behaviour, with distinct properties in the lengthwise and crosswise directions. Since the BEAM181 element formulation admits only a single Young's modulus and a single Poisson's ratio, the lengthwise Young's modulus and the crosswise Poisson's ratio were adopted to characterise the bolt response, consistent with the dominant loading direction along the bolt axis. The temperature-dependent mechanical and thermal properties of G10-CR, evaluated at 22°C, −196°C, and −269°C, are provided in Table 4.4.

Table 3.4: G10-CR fiberglass epoxy temperature-dependent mechanical and thermal properties.

Property	**T = 22 °C**	**T = −196 °C**	**T = −269 °C**
ρ [kg/m^3]	1800	–	–
$E_{\text{lengthwise}}$ [GPa]	28.0	33.7	35.9
$E_{\text{crosswise}}$ [GPa]	22.4	27.0	29.1
$\nu_{\text{lengthwise}}$ [-]	0.150	0.190	0.211
$\nu_{\text{crosswise}}$ [-]	0.144	0.183	0.210
$\alpha_{\text{lengthwise}}$ [μm/(m °C)]	3.06	20.64	20.62
$\alpha_{\text{crosswise}}$ [μm/(m °C)]	3.67	9.17	10.31
$\lambda_{\text{lengthwise}}$ [W/(m °C)]	0.500	0.100	0.025
$\lambda_{\text{crosswise}}$ [W/(m °C)]	0.450	0.080	0.020

Material references: MatWeb fiberglass epoxy datasheet; Mechanical, electrical, and thermal characterisation of G-10CR and G-11CR glass-cloth/epoxy laminates between room temperature and 4 K.

3.4 Split configuration

Both the inner and outer thermal shields are divided into two panels each in the poloidal direction, to mitigate eddy current generation and accommodate thermal contraction. Each panel is independently anchored to the port structure by means of a single fixed bolt and surrounding hinged and non-hinged bolts, arranged in accordance with the bolting scheme described in next section. Two alternative segmentation configurations were examined: the diagonal split and the mid split, which differ in the orientation and position of the parting plane. As each configuration carries inherent advantages and limitations with respect to the load cases, the selection of the appropriate scheme for each port duct was made on the basis of a preliminary study conducted.

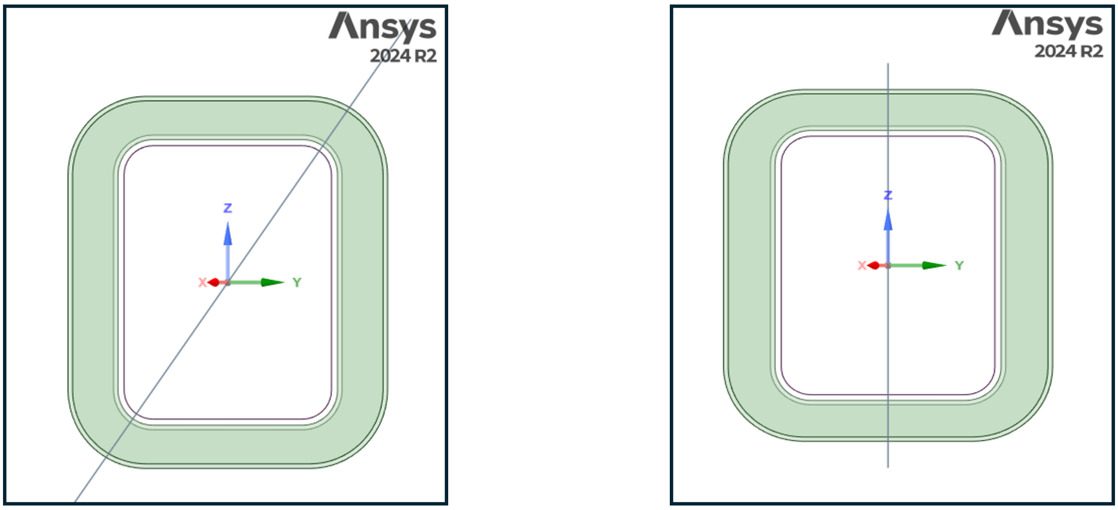

(a) Diagonal split **(b)** Midsplit.

Figure 3.4: Split configurations

In the diagonal split configuration, the fixed bolt is located at the centre of the uncut edge, about which thermal contraction is anchored. The bolt arrangement comprising hinged and non-hinged fasteners is designed such that the thermal displacement field is directed toward this fixed constraint, thereby controlling the contraction path of the shield under cryogenic loading. In contrast to planar structures, which accommodate thermal strain exclusively through uniform, in-plane dimensional contraction, curved shells undergo an intrinsic geometric transformation. Due to non-zero Gaussian curvature ($K \neq 0$), a curved surface cannot scale down uniformly without violating topological constraints or inducing significant membrane energy penalties. Consequently, the shell minimises its internal strain energy by converting uniform thermal contraction into coupled out-of-plane bending and shape distortion. The diagonal split inherently avoids curved cut surfaces, which reduces the complexity of thermal contraction at the parting plane and consequently yields superior performance under thermal loading.

However, as established in Section 4.5.3, the outboard edge of the PTS is left unconstrained and devoid of structural fasteners, resulting in large deformations at the cantilever free edges under gravitational loading. This effect is most pronounced in Port Duct 3, which presents the widest cross-section and a horizontal orientation, both of which maximise the cantilever overhang and the associated deformation. The mid split configuration is therefore introduced as a means of reducing this overhang and mitigating the gravitational deformation at the free edge. The mid-split configuration, defined by a parting plane positioned symmetrically at the mid-height of the C-section flange, was applied to Port Duct 3. Fixed bolt is in web. This configuration was adopted based on comparative deformation study carried out on a geometrically simplified model of Port 3, in which the diagonal and mid split schemes were assessed against each other prior to implementation in the full model. The mid split configuration halves the overhang and therby the deformation.

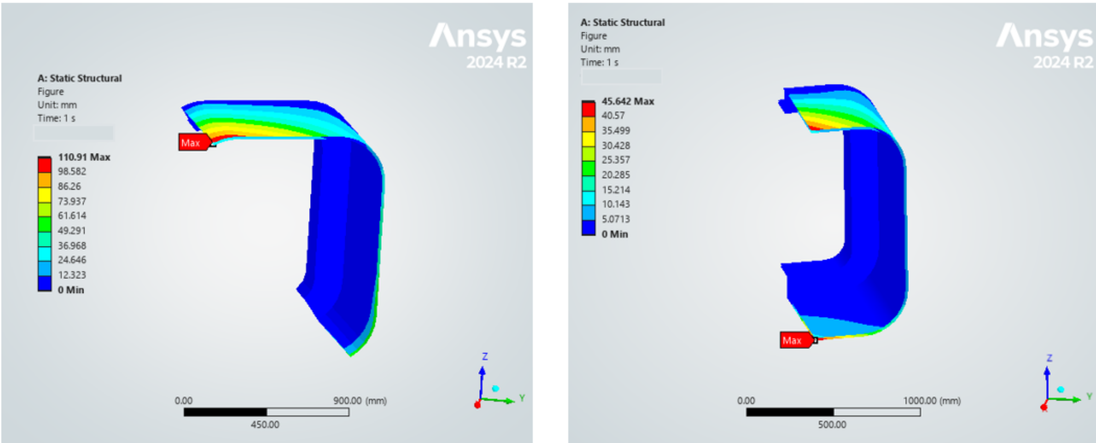

Figure 3.5: Total deformation contours comparing the diagonal split and mid-split configurations for port 3.

Under thermal loading conditions, however, the midsplit configuration produced unfavourable out-of-plane deformations at both flanges. This behaviour is attributed to the location of the fixed bolt on the web. The introduction of no-separation fastener on the flanges was found to effectively minimise this out-of-plane deformation. While the mid-split configuration effectively reduces gravitational deformation in Port 3, the same approach was not extended to Ports 2 and 4, which exhibit similar cantilever behaviour. Given their irregular cross-sectional geometries, introducing a mid-split partition would worsen the deformations under the thermal loading.

As an alternative design consideration, doubling the outer mouth thickness of the Port 3 PTS from 1 mm to 2 mm would significantly increase the local stiffness, reducing the deformation. Structural mechanics dictates self-weight deflection of a flat plate is directly proportional to the ratio of the gravitational load to the flexural rigidity of the component. Because the distributed load increases linearly with thickness while the structural rigidity increases cubically, the resulting deformation follows an inverse-square relationship with thickness. Finite Element Analysis validated this theoretical behavior, demonstrating that doubling the outer wall thickness from 1mm to 2mm reduced the maximum deflection from over 100mm down to less than 27mm.

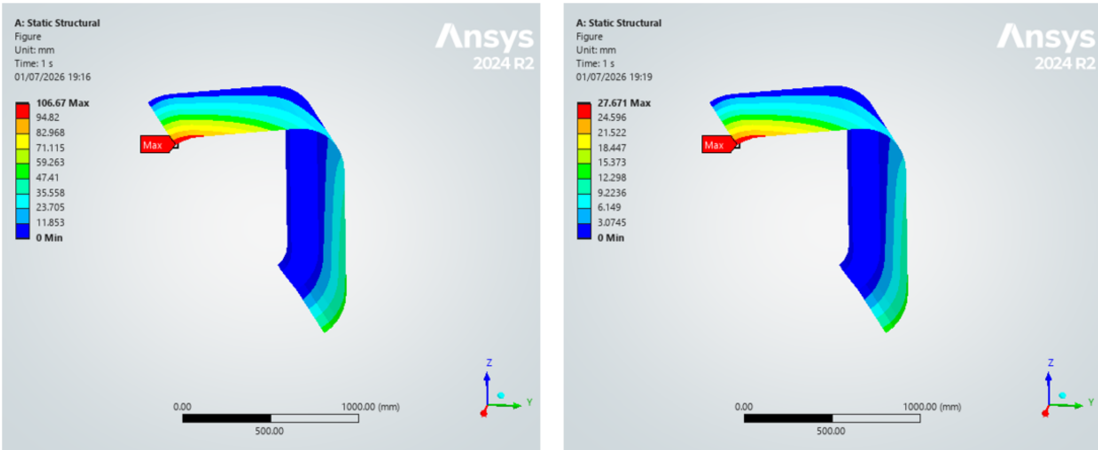

Figure 3.6: Total deformation contours comparing the effect of thickness within the Port 3 diagonal split configuration.

However, since the cooling pipe layout has not yet been finalised, it remains uncertain whether cooling pipes will route through this region, which may impose geometric constraints on any thickness modification. For the purpose of the present analysis, the original geometric configuration is retained in compliance with the current design constraints. Based on structural assessment, the diagonal split configuration was adopted as the standard segmentation scheme for all port ducts. An exception was made for Port Duct 3, for which the mid split configuration was selected, owing to the need to reduce the cantilever overhang and the associated gravitational deformation at the outboard free edge.

3.5 Mechanical scheme of bolt connections

The mechanical coupling between the ports and the port thermal shields (PTS) is realised through a set of G10-CR gravity bolts, whose behaviour was reproduced in the finite element model by means of joint connections and appropriate contact definitions. A single fixed bolt is used as a thermal anchor point. Surrounding fasteners — comprising hinged and non-hinged bolts — are arranged such that the resulting thermal displacement field is directed toward this fixed constraint, ensuring that the contraction path of the shield remains controlled throughout cryogenic cooldown. Three categories of bolt connections were defined, consistent with the mechanical scheme adopted in the literature for analogous thermal shield assemblies:

- Fixed bolts fully suppress relative displacement in both the toroidal and poloidal directions, directly anchoring the PTS to the port structure. These are modelled as bonded connections, permitting no relative motion at the interface.

- Hinged bolts allow relative displacement in either the toroidal or the poloidal direction, but constrain the remaining translational degree of freedom. These connections are modelled with one free translational direction — corresponding to the joint free direction — while the perpendicular in-plane direction remains constrained.

- Non-hinged bolts permit relative displacement in both the toroidal and poloidal directions simultaneously, providing the least kinematic restraint among the three bolt types. These are modelled as no separation joints [11].

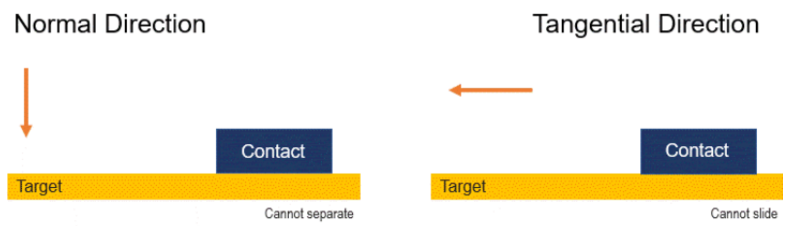

(a) Bonded connection

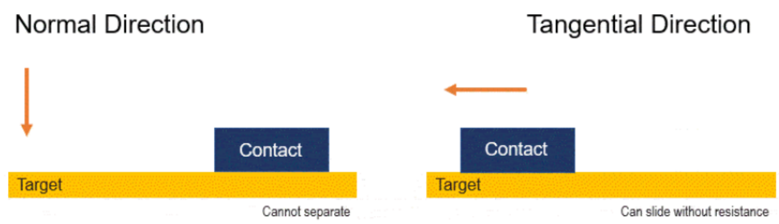

(b) No seperation.

Figure 3.7: ANSYS contact types

All bolts are fixed to the port structure. The bolt connections within the PTS panels are illustrated in Figure 4.5.

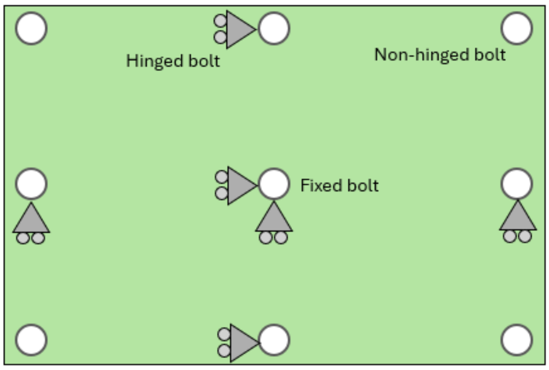

Figure 3.8: Mechanical scheme of bolt connections in a PTS panel

3.6 Bolt layout

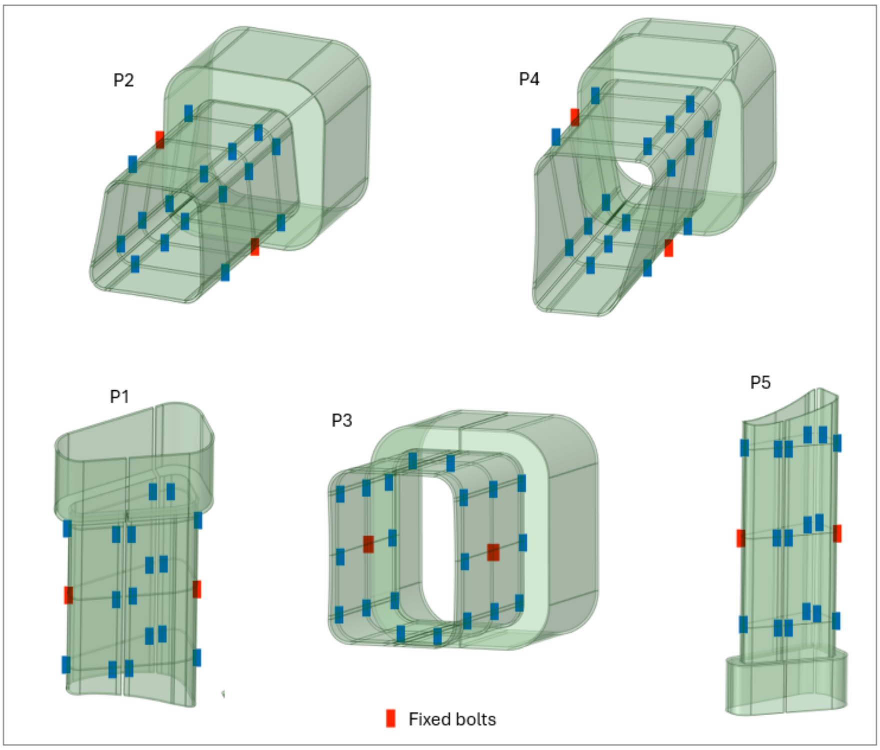

Figure 3.9: Schematic of fixed-bolt positioning

3.7 Boundary conditions

3.7.1 Cyclic Symmetry

Taking advantage of the periodic nature of the 360° assembly, cyclic symmetry boundary conditions were applied at the toroidal cut planes of the 20° sector model. These conditions enforce compatibility of displacements and forces between the two cut faces, ensuring that the sector model accurately represents the behaviour of the full toroidal structure without the computational cost of modelling the entire machine.

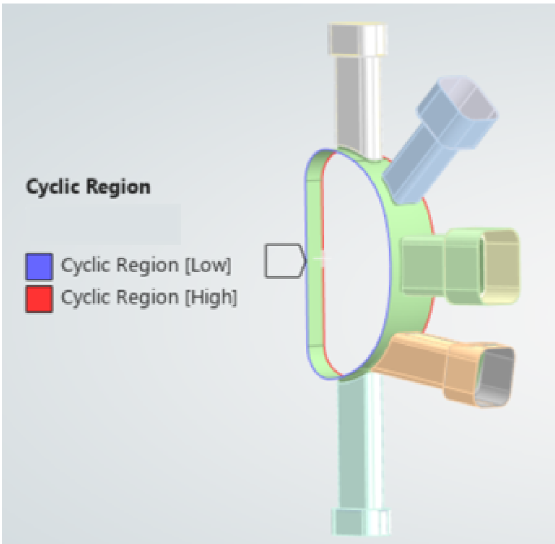

Figure 3.10: 20° sector geometry model

3.7.2 Simply Supported

The lower edge of Port 5, at the interface where it is merged with the vacuum vessel, was assigned a simply supported boundary condition. This constraint suppresses all translational degrees of freedom at the connection edge — representing the attachment of the vacuum vessel to the gravity supports — while leaving rotations free. This is physically consistent with the role of the gravity supports, which carry the dead weight of the assembly while accommodating thermally induced rotations.

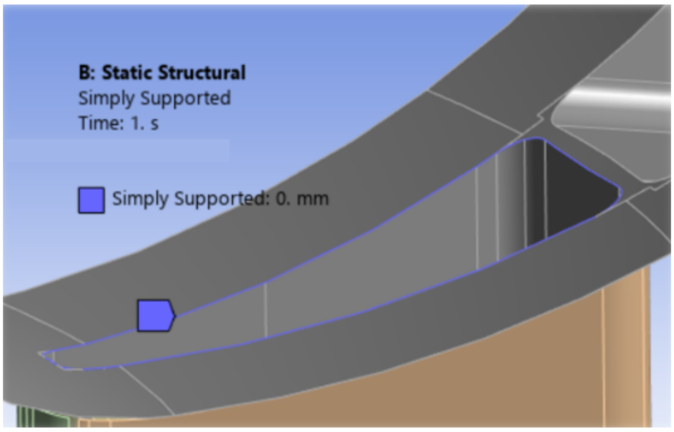

Figure 3.11: simply supported

3.7.3 Outboard Interface Boundary Conditions

The ports of the vacuum vessel are connected to the cryostat ports with bellows to be dimensioned based on loads and temperature ranges. The PTS-CTS interface is achieved through a sliding overlap joint in which the terminal panels of the two shield assemblies telescope into one another. A controlled gap is maintained between the overlapping surfaces, creating a radiation labyrinth geometry that intercepts line-of-sight thermal radiation without establishing direct mechanical contact between the shields, thereby reducing eddy current. Differential thermal displacements between the port and cryostat assemblies, arising from their distinct operating temperature levels during cooldown, are accommodated passively through the mutual sliding of the two panels within the overlap zone, without transmitting significant structural loads across the interface.

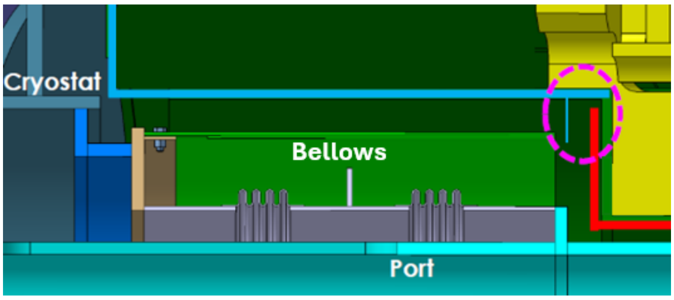

Figure 3.12: Vacuum vessel port- cryostat port interface [8].

At the outboard boundary of the PTS assembly, no structural constraints or bolt connections are imposed in the present model, as this region must remain unobstructed to accommodate the interface mechanisms. This modelling choice reflects the current status of the engineering design, in which the outboard interface conditions have not yet been fully defined. The unconstrained outboard boundary consequently represents a conservative and physically meaningful assumption: it maximises the free deflection at the outboard extremity of the structure, ensuring that the deformation results presented in Chapter 5 represent an upper bound on the structural response under the applied loading conditions.

3.8 Loads

3.8.1 Gravitational load

Standard Earth gravity was applied to the entire model as a body force, with a magnitude of $9806.6\,\mathrm{mm/s^2}$ acting in the negative Z-direction, defined by the component vector $(0, 0, -9806.6)\,\mathrm{mm/s^2}$. This load represents the self-weight of all components, including the ports, PTS, and gravity bolts.

3.8.2 Thermal load conditions

Uniform temperature fields were applied to the model components to reproduce the steady-state thermal environment during machine operation. Transient effects associated with reaching the target temperatures are neglected. The thermal conditions were assigned separately to each component group, reflecting the different operating temperatures across the assembly, and are summarised in Table 4.5.

Table 3.5: Applied thermal conditions by component.

Component	**Temperature [°C]**
Vacuum vessel & ports	+60
Inner thermal shield	−166
Outer thermal shield	−193

The vacuum vessel and ports were assigned a uniform temperature of +60 °C, consistent with the baking operational scenario in which these components are heated to facilitate outgassing of the plasma-facing surfaces. The port thermal shields were assigned temperatures representative of their cryogenic operating conditions: the inner thermal shield was assigned a uniform temperature of −166 °C, while the outer thermal shield was assigned a uniform temperature of −193 °C. These temperature differentials between the structural components give rise to significant differential thermal expansions, which represent the primary source of mechanical loading on the G10-CR gravity bolts connecting the PTS to the ports.

3.8.3 Load cases

Two load cases were considered in the analysis. In Load Case 1 (LC1), only the gravitational body force is active, with no thermal loading applied. This case isolates the structural response due to self-weight alone and provides a baseline for assessing the contribution of thermal effects. In Load Case 2 (LC2), the full thermal condition is applied, representing the most demanding operational scenario in which thermal strains are induced. Thermal strains were computed using a reference temperature of 23 °C, in accordance with the material definitions described in Section 3.3.

3.9 Mesh Generation

The finite element mesh was generated using the default meshing settings available in ANSYS Mechanical, with linear element order adopted throughout. Both adaptive and uniform global sizing options were disabled, preserving local topological fidelity without introducing unnecessary element inflation. The element size was selected on the basis of a mesh convergence study, ensuring that the chosen discretisation yielded results independent of further mesh refinement while maintaining reasonable computational cost. All other meshing parameters were retained at their default settings, including the default curvature and proximity capture settings, which ensured adequate resolution of geometric features without the need for additional manual refinement. Mesh quality was verified using the Aggressive Mechanical error limit setting, with medium smoothing applied throughout. No manual inflation layers or local size fields were introduced, consistent with the shell- and beam-dominated nature of the geometry.

3.10 Mesh Verification and Grid Independence

A mesh convergence study was conducted to verify that the finite element results are independent of spatial discretisation. The Port 3 PTS assembly was selected as the representative model for this study, given that it presents the most geometrically complex configuration and the largest deformation magnitudes among the five port assemblies. The analysis was performed across nine mesh refinements, with element sizes ranging from 60 mm to 20 mm, evaluating convergence based on the maximum total deformation under both gravity (LC1) and thermal (LC2) load cases.

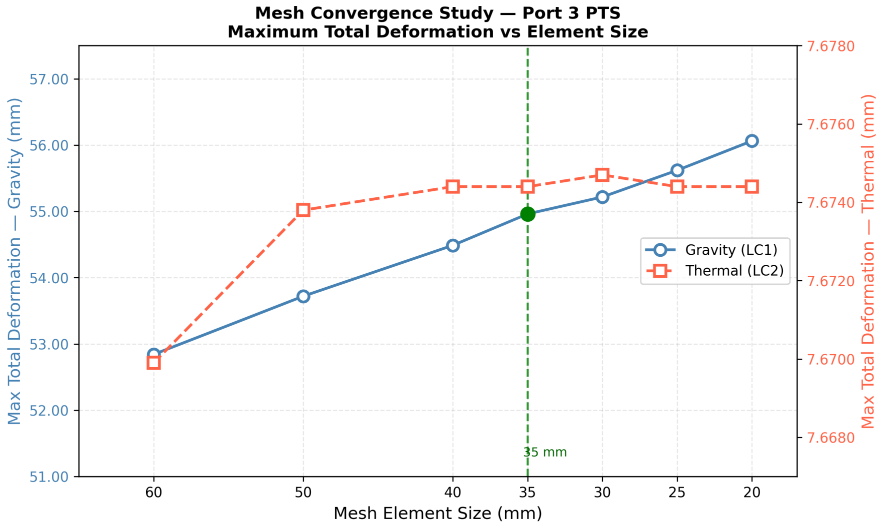

Figure 3.13: Mesh convergence study

The thermal deformation response (LC2) demonstrated immediate mesh independence, exhibiting a peak-to-peak variation of less than 0.07% (0.005 mm) across the entire range of element densities tested. This behaviour is physically expected, as thermal deformation in an unconstrained structure is governed entirely by differential thermal expansion and is inherently insensitive to mesh density. The gravity deformation response (LC1) exhibited a consistent monotonic trend with increasing mesh refinement, approaching a horizontal asymptote as the element size decreased below 40 mm. At the selected mesh density of 35 mm, the maximum total deformation is 54.961 mm. Further refinement to 20 mm yields a maximum total deformation of 56.063 mm, representing a variation of approximately 2.0% relative to the 35 mm result. This residual variation is attributed to localised mesh sensitivity at geometric interfaces and contact boundaries, which is characteristic of contact-dominated structural problems. The global load paths and macro-level structural response are considered fully converged at the 35 mm mesh density.

Based on these results, a 35 mm global element size was adopted as the operational mesh baseline for all analyses. Due to the geometric similarity and identical structural assembly principles shared across all five port configurations, the convergence study was not repeated for the remaining models. The verified 35 mm mesh density, combined with curvature-based local refinement at geometric discontinuities, was applied uniformly across all port assemblies, ensuring equivalent discretisation quality and numerical independence throughout the study without incurring unnecessary computational overhead.

3.11 Analytical Verification

3.11.1 Thermal Contraction and Thermal Stress

As a first analytical verification, the thermal contraction of a straight edge of the Port 1 outer PTS panel was compared against the corresponding finite element result. Under cryogenic operating conditions, the PTS assembly is cooled from the reference temperature of $T_{\mathrm{ref}} = 23\,^\circ\mathrm{C}$ to an operating temperature of $T_{\mathrm{op}} = -193\,^\circ\mathrm{C}$, resulting in a temperature differential of $\Delta T = 216\,^\circ\mathrm{C}$. The thermal contraction of a free elastic bar is given by:

$$\delta = \alpha \cdot \Delta T \cdot L \tag{3.1}$$

where α is the coefficient of thermal expansion, ΔT is the applied temperature differential, and L is the length of the edge under consideration. A straight vertical edge of the port duct structure was selected for this comparison, with a measured length of $L = 2187.6\,\mathrm{mm}$. At the operating temperature of $-193\,^\circ\mathrm{C}$, the thermal expansion coefficient of AISI 316LN is taken as $\alpha = 13.3\,\mu\mathrm{m}/(\mathrm{m}\cdot{}^\circ\mathrm{C})$ in accordance with the material data presented in Table 3.3. Substituting into Equation 3.1:

$$\delta_{\mathrm{analytical}} = 13.3 \times 10^{-6} \times 216 \times 2187.6 = 6.285\,\mathrm{mm} \tag{3.2}$$

The corresponding deformation was extracted from the finite element model by evaluating the directional deformation along the Z-axis on the same edge. The net thermal contraction obtained from the FEA, computed as the difference between the maximum and minimum nodal displacements along the edge, was found to be:

$$\delta_{\mathrm{FEA}} = 5.4113 - (-0.45058) = 5.862\,\mathrm{mm} \tag{3.3}$$

The percentage difference between the analytical and FEA results is:

$$\epsilon = \frac{|\delta_{\mathrm{analytical}} - \delta_{\mathrm{FEA}}|}{\delta_{\mathrm{analytical}}} \times 100 = \frac{|6.285 - 5.862|}{6.285} \times 100 = 6.7\% \tag{3.4}$$

The discrepancy of 6.7% is considered acceptable and is physically expected. The analytical formula assumes a fully unconstrained bar undergoing uniform thermal contraction, whereas in the finite element model the edge forms part of a continuous structural assembly. The close agreement between the two solutions confirms that the finite element model captures the thermal contraction behaviour of the PTS assembly with sufficient accuracy for the purposes of this study.

Further qualitative verification is provided by the thermal stress distribution. Since the PTS panel is free to contract without structural restraint, supported only at the fixed bolts. This is confirmed by the finite element results, in which the von Mises equivalent stress across the PTS panel under thermal loading is effectively zero. This behaviour is fully consistent with the theoretical expectation for a thermally loaded structure with unconstrained boundary conditions, providing additional confidence in the correctness of the model setup.

3.11.2 Bolt Reaction Force

As a second verification check, the reaction force carried by the bolts in gravity loading was compared against an analytical static equilibrium calculation. Port 1 and Port 5 have a pure vertical orientation, such that the gravity load acts perpendicular to the bolt axis, loading the bolts in pure transverse shear with no axial force component. This configuration provides a straightforward and unambiguous basis for analytical verification.

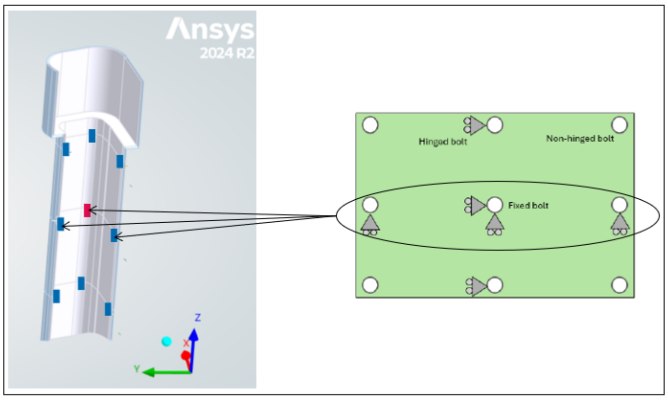

Figure 3.14: Port 1 PTS panel selected for bolt force verification.

As illustrated in Figure 3.14, the bolt connection scheme adopted for the selected PTS panels from Port 1 assigns the entire gravitational weight of both the outer and inner PTS panels to the three bolts in the middle row. So, the bolt in the middle row can therefore be idealised as a cantilever beam, fixed at the port duct wall and loaded by two transverse point loads at positions corresponding to the attachment locations of the outer and inner PTS panels respectively, as shown in Figure below.

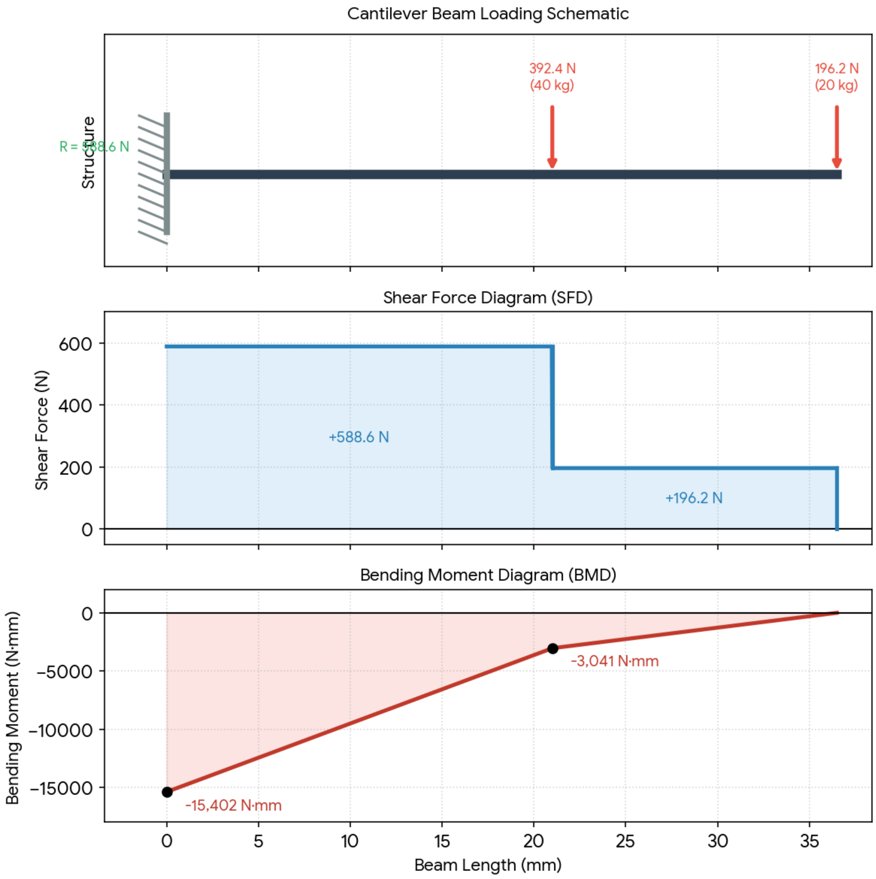

Figure 3.15: Cantilever beam idealisation of bolt under consideration and corresponding shear force diagram.

Applying static equilibrium to this idealised cantilever configuration, the total vertical reaction at the fixed support must equal the combined gravitational weight of the two PTS panels:

$$R = W_{\text{total}} = (m_{\text{outer}} + m_{\text{inner}}) \times g = (20.7 + 39.3) \times 9.81 = 588.4\,\text{N} \tag{3.5}$$

where $m_{\text{outer}} = 20.7\,\text{kg}$ and $m_{\text{inner}} = 39.3\,\text{kg}$ are the masses of the outer and inner PTS panels respectively. The shear force diagram (SFD) corresponding to this loading configuration is presented in Figure 3.15, confirming the analytical reaction force of 588.4 N at the fixed end.

This total reaction force is shared among the three bolts in the middle row. It is noted that the individual reaction force carried by each bolt is not necessarily equal, as the actual load distribution depends on the geometric eccentricity. Therefore, the sum of reaction forces across all three bolts are used as the verification criterion.

Since the bolt beam elements are connected to shell elements at the port duct wall, a direct force reaction probe could not be scoped to the bolt connection. The total shear force at the fixed end of each bolt beam element was therefore extracted using the Beam Tool in ANSYS Mechanical, which is equivalent to the vertical reaction force at the support for a cantilever configuration. The sum across the three bolts was found to be:

$$V_{\text{FEA, total}} = 587.9\,\text{N} \tag{3.6}$$

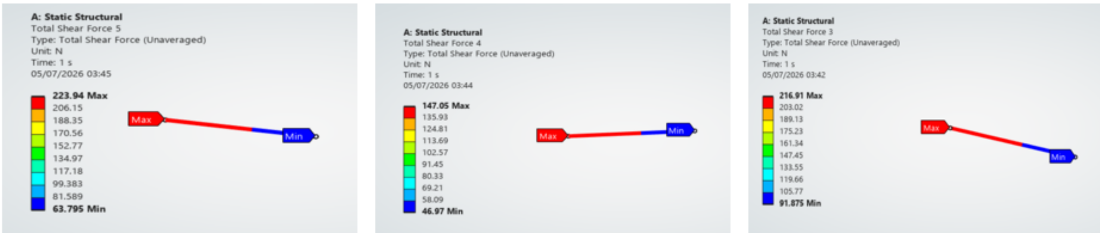

Figure 3.16: Shear forces in beams.

The percentage difference between the analytical and FEA results is:

$$\epsilon = \frac{|588.4 - 587.9|}{588.4} \times 100 = 0.1\% \tag{3.7}$$

The agreement of 0.1% is excellent and confirms that the gravity load is correctly applied in the finite element model and that the bolt beam elements accurately capture the total vertical load transfer through the bolted interface. This result provides strong confidence in the correctness of the boundary condition implementation and the load transfer mechanism modelled between the PTS panels and the port duct structure.

The force equilibrium is checked independently of force positions; the bending reaction moment remains completely dependent on the exact spatial location of each load relative to the fixed boundary. The rigid cantilever idealisation simplifies the panel weight into discrete point loads at assumed attachment points. In reality, the PTS panel is a flexible, geometrically complex, non-uniform, thin-walled structure that deforms under gravity and rotates about its bolt connections. This rotational behavior is clearly demonstrated by the development of axial forces within the non-separation bolts of the upper and lower rows. Therefore, the analytical bending moment value serves merely as an order-of-magnitude reference.

3.11.3 Beam deflection

For the cantilever tip deflection verification, the same simplified cantilever idealisation is adopted. Assuming the three bolts share the total panel weight equally, each bolt carries one-third of the gravitational load of each PTS panel:. The applied loads per bolt are therefore:

$$P_1 = \frac{m_{\text{outer}} \times g}{3} = \frac{20.7 \times 9.81}{3} = 67.7\,\text{N} \quad (\text{Outer PTS, at } a = 21\,\text{mm}) \tag{3.8}$$

$$P_2 = \frac{m_{\text{inner}} \times g}{3} = \frac{39.3 \times 9.81}{3} = 128.4\,\text{N} \quad (\text{Inner PTS, at } L = 36.5\,\text{mm}) \tag{3.9}$$

- Diameter: $d = 10$ mm
- Second moment of area: $I = \dfrac{\pi d^4}{64} = 490.87$ mm^4
- Elastic modulus: $E = 33{,}700$ MPa (G10-CR at cryogenic temperature)
- Bolt length: $L = 36.5$ mm

Applying the principle of superposition, the analytical tip deflection is:

$$\delta_1 = \frac{P_1 a^2}{6EI}(3L - a) = \frac{67.7 \times 21^2}{6 \times 33700 \times 490.87}(3 \times 36.5 - 21) = 0.0267\,\text{mm} \tag{3.10}$$

$$\delta_2 = \frac{P_2 L^3}{3EI} = \frac{128.4 \times 36.5^3}{3 \times 33700 \times 490.87} = 0.1258\,\text{mm} \tag{3.11}$$

$$\delta_{\text{analytical}} = \delta_1 + \delta_2 = 0.0267 + 0.1258 = 0.1525\,\text{mm} \tag{3.12}$$

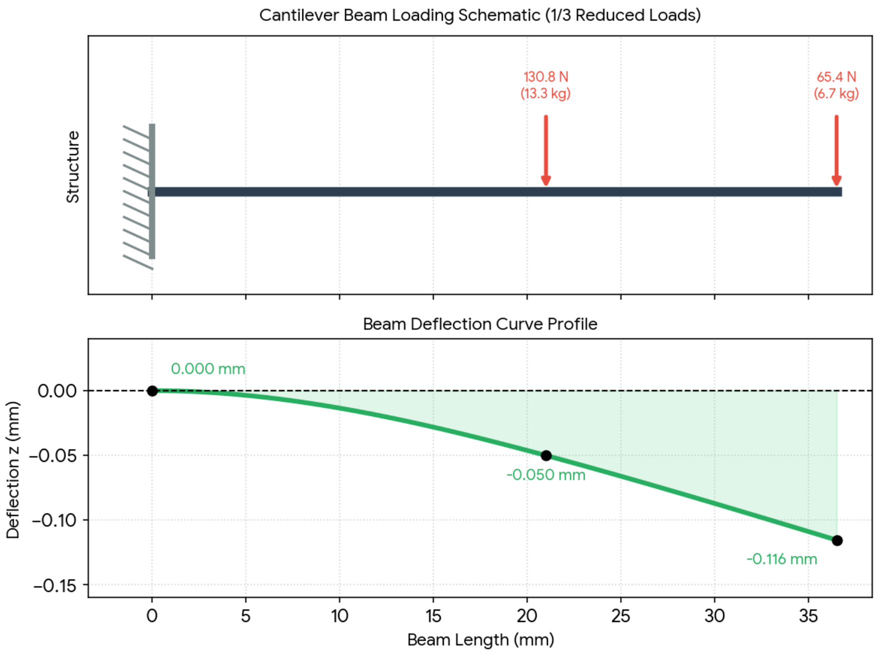

Figure 3.17: Deflection of idealized cantilever beam.

The corresponding deflection was extracted from the finite element model as the relative directional deformation between the root and tip nodes of the bolt beam element:

$$\delta_{\text{FEA}} = |\delta_{\text{tip}} - \delta_{\text{root}}| = |-0.44653 - (-0.36422)| = 0.0823\,\text{mm} \tag{3.13}$$

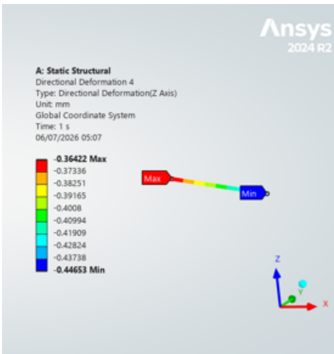

Figure 3.18: Deflection of beam.

The percentage difference between the analytical and FEA results is:

$$\epsilon = \frac{|\delta_{\text{analytical}} - \delta_{\text{FEA}}|}{\delta_{\text{analytical}}} \times 100 = \frac{|0.1525 - 0.0823|}{0.1525} \times 100 = 46\% \tag{3.14}$$

Similar to bending, deflection also depends on the exact loading; the analytical calculation derived from the simplified cantilever model serves as a reference value. The displacement results obtained via finite element analysis (FEA) show strong order-of-magnitude agreement with this analytical prediction, successfully confirming the fundamental validity of the computational setup.

In summary, the analytical verifications presented in this section provide a comprehensive assessment of the finite element model's reliability across thermal and structural load cases. The thermal contraction check showed close agreement between the analytical and FEA results, with a discrepancy of 6.7%, attributable to the additional structural continuity present in the finite element model relative to the idealised free bar. The bolt reaction force verification yielded excellent agreement, with a discrepancy of only 0.1%, confirming the correct implementation of the gravity load path and boundary conditions at the bolted interface. The beam deflection check, while showing a larger discrepancy of 46%, remains consistent with the simplifications inherent in the rigid cantilever idealisation, which does not capture the true rotational and eccentric loading behaviour of the panel. In addition, symmetry of the results was checked across corresponding features of the model, and the obtained values were found to lie within the same order of magnitude, further supporting the internal consistency of the solution. Taken together, these independent checks, spanning thermal, force, and displacement quantities, are considered to be in good overall agreement with the analytical reference calculations, thereby providing confidence in the correctness of the modelling assumptions, boundary conditions, and load transfer mechanisms adopted throughout the finite element analysis of the PTS assembly.

Chapter 4

Results and Conclusions

The objective of these analyses is to assess the deformation of the ports and PTS under structural and thermal load conditions and to evaluate the relative distances (gaps) between ports, inner THS and outer THS.

To manage the geometric complexity and large physical scale of the complete DTT sector, each PTS was analysed individually. Rather than simulating the entire PTS assembly simultaneously, each PTS was analysed separately. This approach is computationally efficient and significantly reduces computational time while still capturing the relevant structural behaviour. For thermal load cases, this assumption is exact, as thermal strain is unaffected by the mass of adjacent PTS structures. For the gravity load case, the mass contribution of the remaining PTS structures was initially considered as an added distributed mass applied to the corresponding port duct; however, their inclusion was seen as insignificant during initial analysis. This outcome is expected, given that PTS panels are way lighter than the combined port duct and vacuum vessel structure. Therefore, the adjacent PTS masses were neglected in all subsequent analyses, and each PTS was treated as fully independent.

4.1 Total deformation

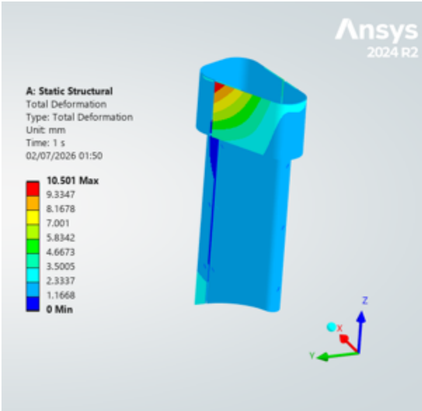

(a) Port 1

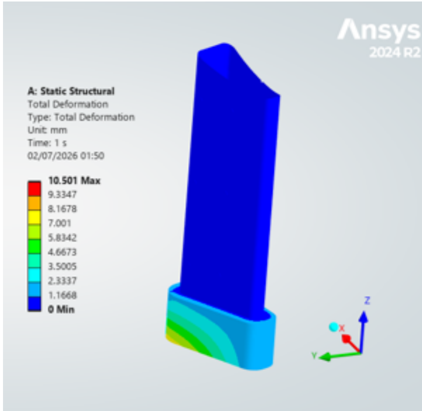

(b) Port 5

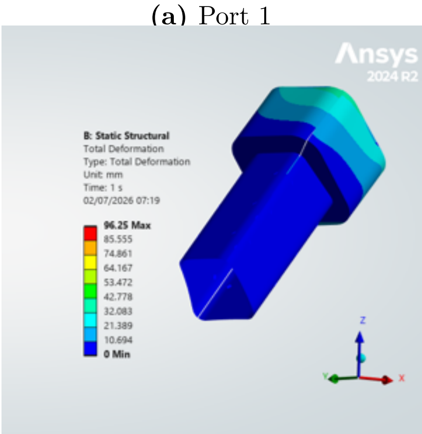

(c) Port 2

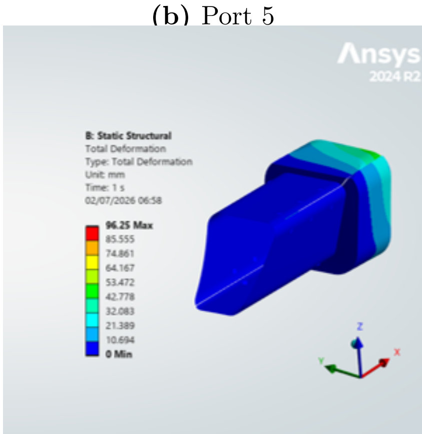

(d) Port 4

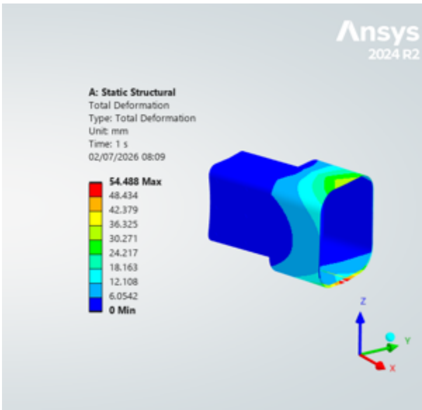

(e) Port 3

Figure 4.1: PTS panel displacement field under gravity (LC1). Units: mm

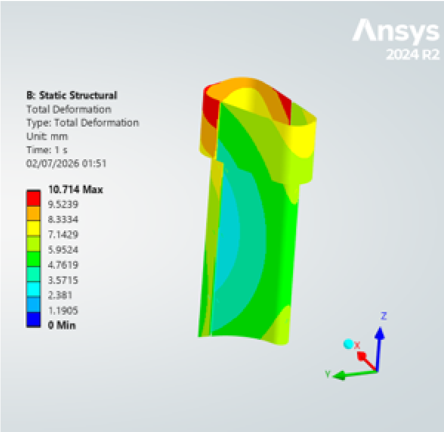

(a) P1

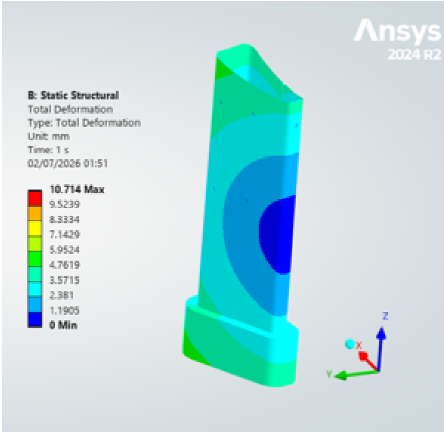

(b) P5

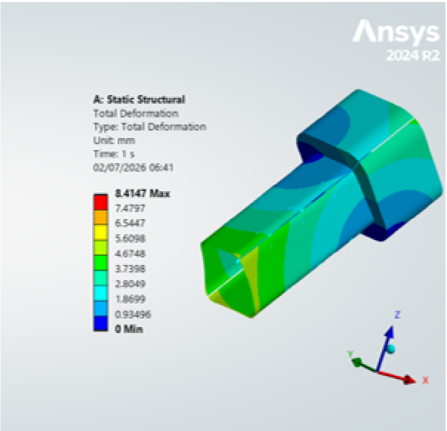

(c) P2

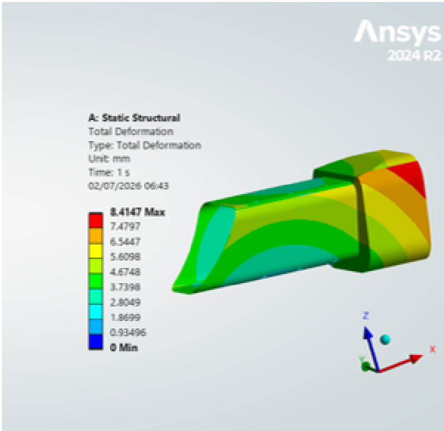

(d) P4

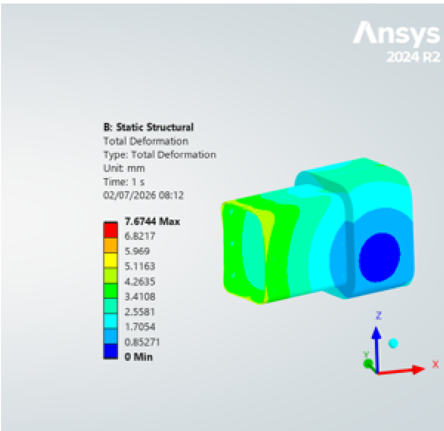

(e) P3

Figure 4.2: PTS panels displacement field under thermal loads (LC2). Units: mm

The PTS assembly exhibits maximum displacements ranging from 2 mm to 96 mm under gravity loading and from 2 mm to 10 mm under thermal loading, confirming the structural integrity of the PTS assembly under the imposed load conditions. The deformation pattern is consistent across all analysed scenarios: displacements in the inboard duct region are relatively modest, ranging from 1 mm to 6 mm, owing to the adequate bolt connections to the port duct which provide effective restraint. In contrast, significantly larger deformations are observed in the outboard peripheral region, where the absence of bolt attachments and the lack of boundary conditions result in a cantilever-like response, amplifying the free-edge displacements under both gravity and thermal loading.

4.2 Von Mises equivalent stress distribution

The von Mises equivalent stress levels in the PTS panels remain well within acceptable limits across all analysed load cases. Under thermal loading, stresses are negligible, as the PTS is free to expand without significant restraint, resulting in minimal stress build-up. Under gravity loading, stress concentrations are observed primarily at the neck region of the PTS and in the immediate vicinity of the bolt connections, which is physically consistent with the expected load transfer paths through the bolted support interface.

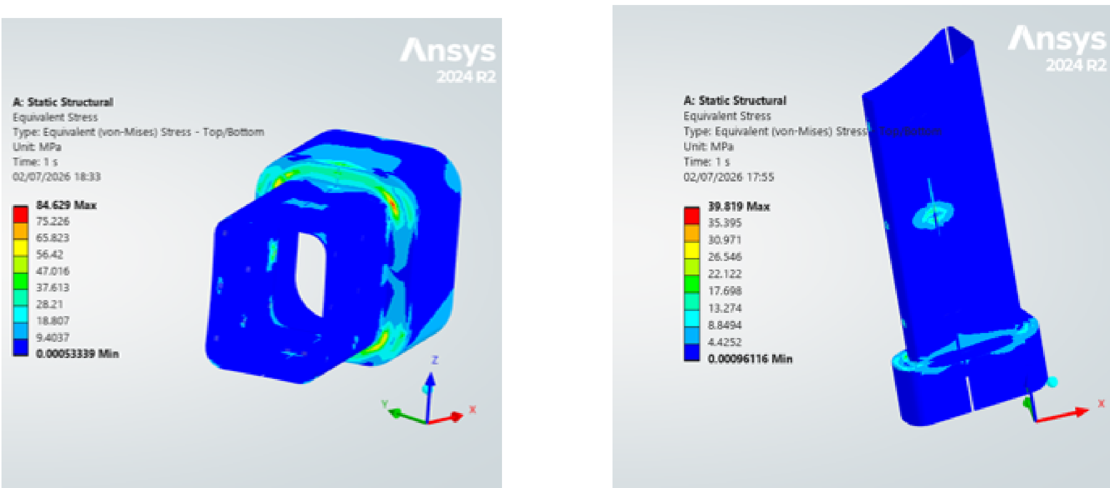

Figure 4.3: Von Mises equivalent stress distribution in Port 3 and Port 5 PTS panels under gravity loading (LC1). Units: MPa

4.3 Gap distribution between the PTS outer and PTS inner contact surfaces

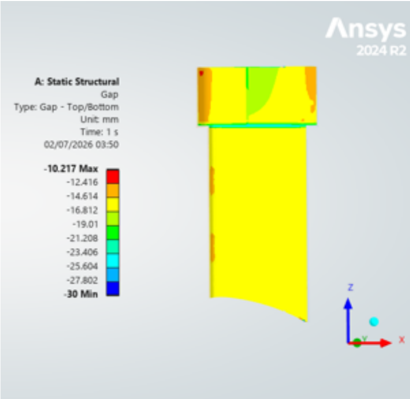

(a) P1

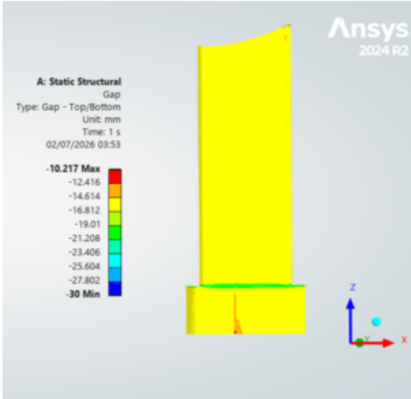

(b) P5

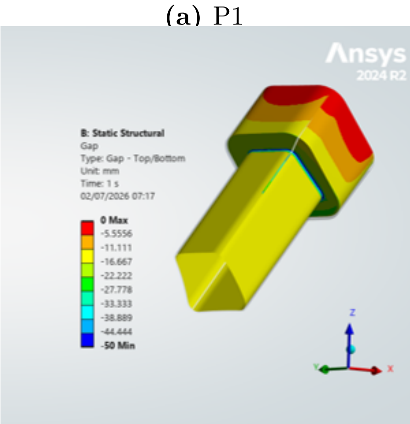

(c) P2

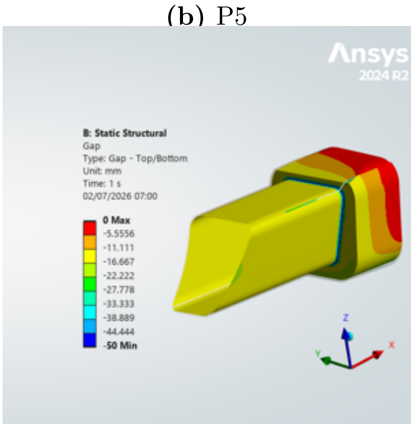

(d) P4

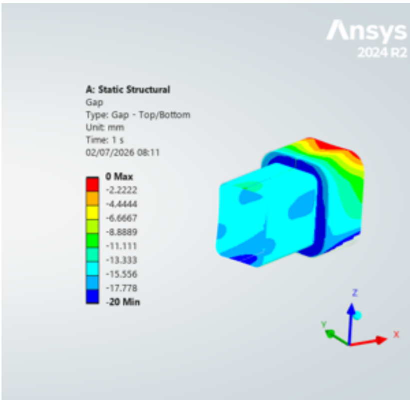

(e) P3

Figure 4.4: Gap between the PTS outer and PTS inner under gravity (LC1)

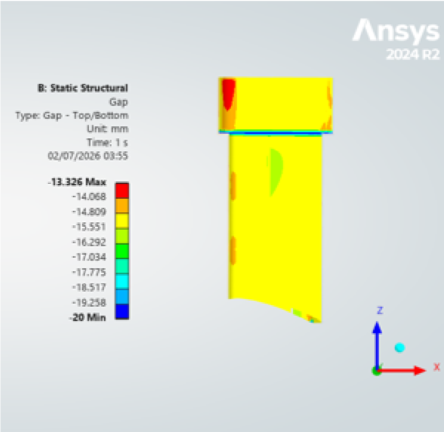

(a) P1

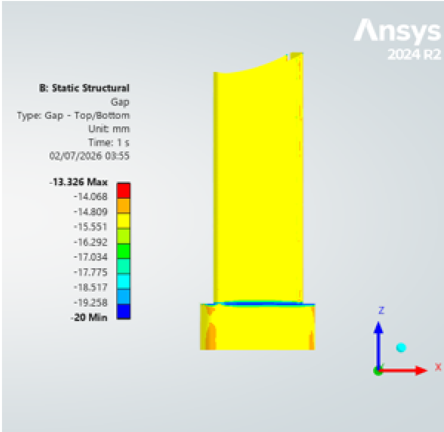

(b) P5

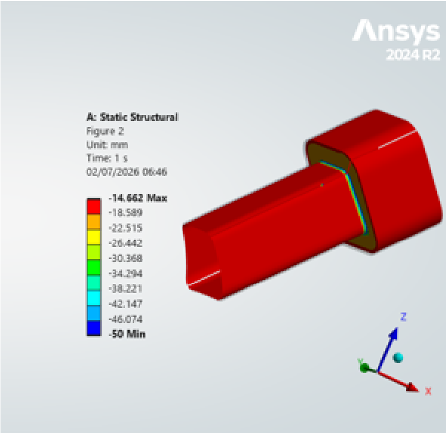

(c) P2

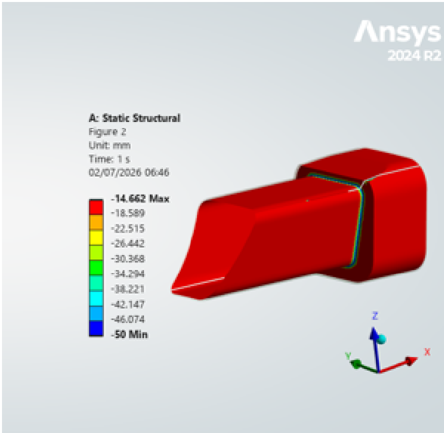

(d) P4

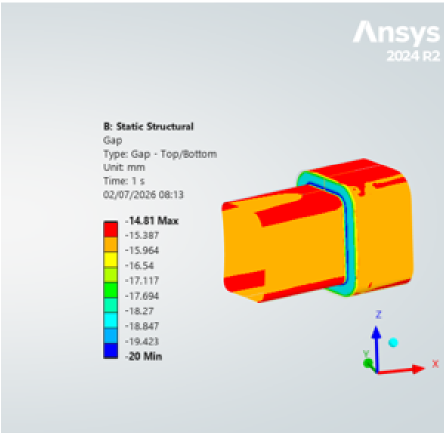

(e) P3

Figure 4.5: Gap between the PTS outer and PTS inner under thermal load (LC2)

4.4 Gap distribution between the port duct and PTS inner contact surfaces

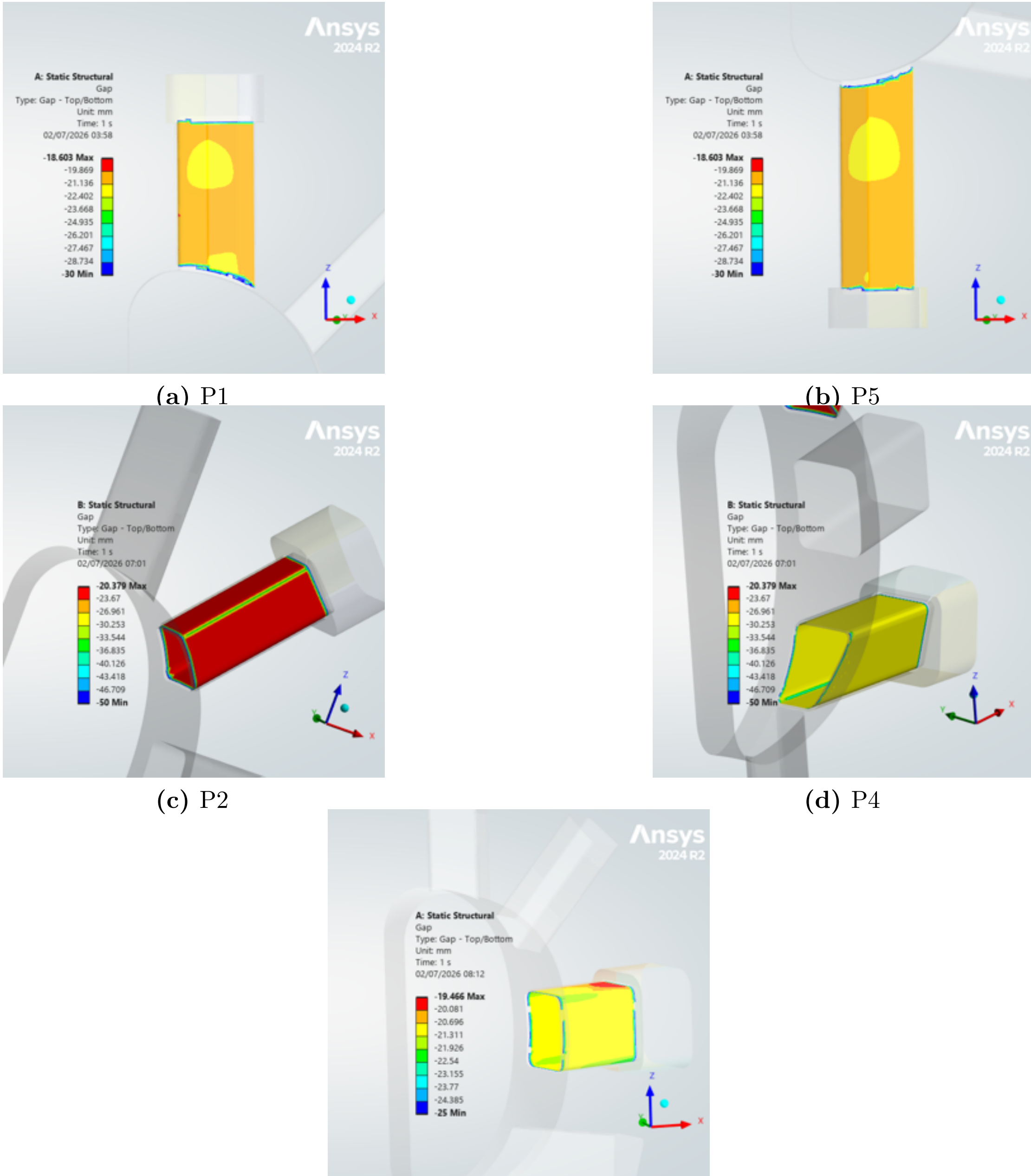

(a) P1 **(b)** P5 **(c)** P2 **(d)** P4 **(e)** P3

Figure 4.6: Gap between the port duct and PTS inner under gravity (LC1)

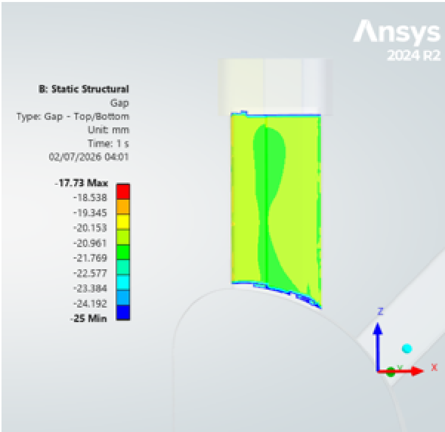

(a) P1

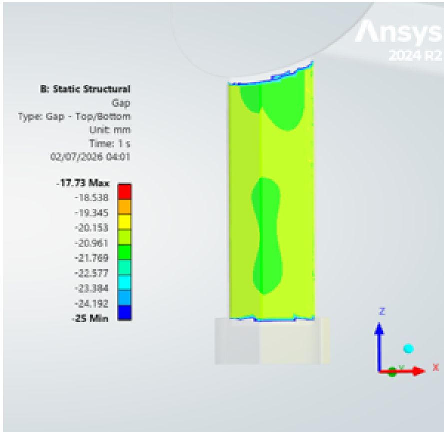

(b) P5

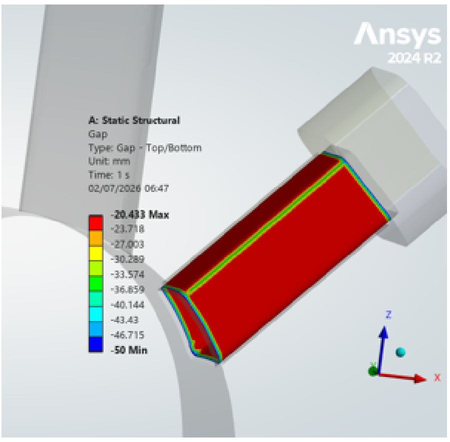

(c) P2

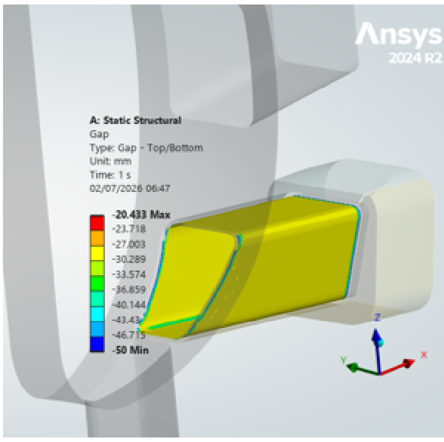

(d) P4

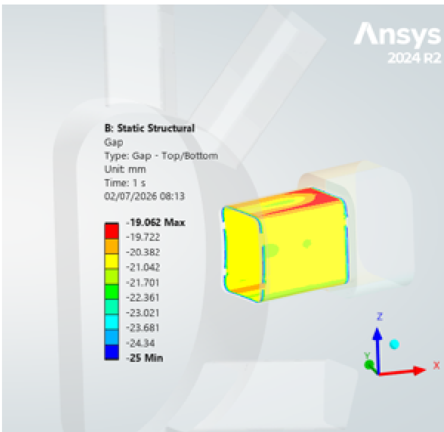

(e) P3

Figure 4.7: Gap between the port duct and PTS inner under thermal loads (LC2)

One of the key outcomes of the analysis is the evaluation of the relative distances between the port duct, inner THS, and outer THS, which are critical for ensuring that no local contact areas form due to thermal deformations. Such contact could compromise the operability and functionality of the system. As shown in Figs. 5.8, the gap between the inner THS and the outer THS remains virtually unchanged from its initial value of 15.5 mm. Similarly in Figs. 5.10, the gap between port duct and the inner THS is unchanged from its initial value of 21 mm all ports except port 4 where its undeformed nominal gap is 27mm.

Under gravity loading, the inboard duct region maintained adequate gap clearances across all ports. However, gap closure was observed in the outboard peripheral region, where the absence of structural constraints results in large free-edge deformations, as discussed in the preceding sections.

4.5 Evaluation of bolt stresses using beam element results

The stresses within the bolts were evaluated using beam tool results. The assessment included the determination of direct axial stresses as well as the maximum and minimum combined stresses. Across all analyzed load cases, the resulting stresses are remarkably low, reaching a peak value of only 60 MPa. This maximum stress sits well below the allowable limits of G-10 CR composite, which exhibits ultimate strengths exceeding 600 MPa at cryogenic operating temperatures. While this simplified beam model successfully captures the global structural response, it cannot resolve local stress fields. In the physical components, true stress distributions will vary, and localized peak stresses will occur at thread and boundary interfaces. However, the low nominal stress of 60 MPa confirms that the fasteners operate with a high safety margin, ensuring global structural integrity under the prescribed loading conditions.

4.6 Conclusions

This study investigated the thermo-mechanical behaviour of the Thermal Shield (THS) components in the Divertor Tokamak Test (DTT) system under thermal and mechanical loading scenarios. Key objectives included evaluating displacement and stress distributions in the port ducts, inner THS, outer THS and bolts, as well as examining the relative distances (gaps) between the three shells.

The PTS are segmented into two separate panels bolted to the port duct using a combination of fixed, hinged, and non-hinged fasteners. The fixed bolt functions as a thermal anchor. The surrounding hinged and non-hinged bolts are arranged to guide the thermal displacement field toward this fixed constraint, maintaining a controlled contraction path for the PTS panel. The structural response of the assembly was comprehensively investigated under both gravity and thermal loading conditions. Across all evaluated ports and loading conditions, the inboard duct region exhibited consistent displacement profiles. In contrast, gravity loading induced excessive deformations within the outboard overhanging mouths of the PTS. This behaviour is attributed to the robust bolted connections in the duct region and complete absence of structural constraints at the outboard PTS–CTS interface in the current design phase. Although doubling the wall thickness in this outboard mouth region could theoretically reduce these displacements fourfold, this study maintained the original design dimensions. Instead, an alternate split configuration was adopted on the port most sensitive to this deformation. The analysis reveals that a diagonal split effectively constrains thermal out-of-plane displacements, since a diagonal split inherently avoids the curved section of the PTS panels and allows planar thermal contraction.

The number and arrangement of the bolted connections proved completely adequate for maintaining structural integrity, ensuring that critical stress thresholds were never reached in either the panels or the bolts. Instead, significant stresses were strictly confined to the vacuum vessel near its simply supported edges. The model neglects the bolts' own thermal strain, since capturing their precise internal temperature distribution would require a coupled thermal analysis beyond the scope of this work. While this simplification is reasonable given the small physical size of the bolts, the thermal stresses induced by internal temperature gradients cannot be dismissed on the same basis, as even a modest gradient across a short, constrained length can generate significant local stress. A more comprehensive local stress assessment would therefore require a solid-element representation of the bolt geometry, incorporating bolt preload and thermal boundary conditions derived from a coupled thermal-structural analysis. Accordingly, absolute stress values obtained under the thermal load case should be interpreted with appropriate caution, and this is identified as an area for future refinement. Relative gaps between the VV, inner THS, and outer THS were largely maintained, with only minor variations. The analysis confirmed that no contact occurs between the shells under the imposed thermal loads, preserving the system's operability.

Future studies should explicitly model the cooling pipes in the structural analysis to accurately determine localised thermal-stress interactions. Furthermore, modelling the bolts using beam elements represents a simplified approach that is useful only for understanding the global behaviour of the structure and the macro-level interactions between components; consequently, high-fidelity models must be employed in subsequent iterations to fully capture the true, localized structural behaviour and to validate the localized stress fields. This fidelity upgrade will be supported by refining the steady-state thermal assumption with transient models to validates the thermal physics. Finally, the temperature-dependent material definitions implemented for the G10-CR composite must be validated further, particularly within regimes where numerical data interpolation was required due to a current lack of empirical material testing data.

Bibliography

[1] ITER Organization. *ITER – the way to new energy*. 2025. URL: `https://www.iter.org/` (visited on 06/16/2026) (cit. on pp. 3, 7, 12).

[2] L Affinito et al. «DTT divertor tokamak test facility–interim design report». In: *DTT Divertor Tokamak Test facility–Interim Design Report*. ENEA Italian National Agency for New Technologies, 2019 (cit. on p. 18).

[3] Gianluca Barone, Selanna Roccella, Emanuela Martelli, and Eliseo Visca. «DTT thermal shield: Preliminary thermal analysis». In: *Fusion Engineering and Design* 158 (2020), p. 111725 (cit. on p. 19).

[4] Kwanwoo Nam et al. «Thermal analysis on detailed 3D models of ITER thermal shield». In: *Fusion Engineering and Design* 89.7-8 (2014), pp. 1843–1847 (cit. on p. 21).

[5] V Bykov, A Nishikawa, G Dalle Carbonare, A Alekseev, S Grigoriev, Yu Krasikov, V Krylov, A Labusov, and M Nakahira. «The thermal shields for the ITER magnet system: thermal, structural and assembly aspects». In: *Fusion engineering and design* 58 (2001), pp. 177–182 (cit. on p. 25).

[6] Shigetoshi Nakamura, Yusuke Shibama, Shinji Sakurai, Junnichi Yagyu, Fuminori Okano, Koji Kamiya, Go Matsunaga, Kei Masaki, and Akira Sakasai. «Design and manufacturing of thermal shield for JT-60SA». In: *Fusion Engineering and Design* 146 (2019), pp. 2375–2378 (cit. on p. 25).

[7] K. Kamiya and Y. Onishi. *Detailed Analysis Report of Thermal Shield for JT-60SA – WBS 19*. Technical Report JT60SA-JA-5801-0. Japan Atomic Energy Agency (JAEA), Oct. 2012 (cit. on p. 27).

[8] R. Bonifetto et al. «Design of the thermal shield for the DTT facility». In: *33rd Symposium on Fusion Technology (SOFT 2024)*. Poster ID P3-101. Dublin, Ireland, Sept. 2024 (cit. on pp. 28, 29, 47).

[9] S Del Nero, M Fulici, G Barone, R Bonifetto, M Dalla Palma, and P Fanelli. «Thermo-mechanical analysis of DTT Vacuum Vessel Thermal Shield». In: *Fusion Engineering and Design* 216 (2025), p. 115090 (cit. on pp. 30, 31, 33).

[10] *ANSYS Mechanical APDL Element Reference*. Release 2021 R2. ANSYS, Inc. Canonsburg, PA, 2021. URL: `https://www.ansys.com` (cit. on p. 36).

[11] *ANSYS Mechanical APDL Theory Reference*. Release 2021 R2. ANSYS, Inc. Canonsburg, PA, 2021. URL: `https://ansys.com` (cit. on p. 44).

List of Abbreviations

1. Reactor Components & Systems

CPs Cooling Pipes

CS Central Solenoid

CTS Cryostat Thermal Shield

EF Equilibrium Field

MLI Multi-Layer Insulation

PF Poloidal Field

PTS Port Thermal Shield

STS Support Thermal Shield

TF / TFC Toroidal Field / Toroidal Field Coil

THS / TS Thermal Shield / Thermal Heat Shield

TTS Transition Thermal Shield

VV Vacuum Vessel

VVTHS Vacuum Vessel Thermal Heat Shield

VVTS Vacuum Vessel Thermal Shield

2. Engineering, Modeling & Software Terms

BAK Baking Phase

BEAM188 Linear beam element type in ANSYS software

CAD Computer-Aided Design

EM Electro-magnetic

FE Finite Element

FEA Finite Element Analysis

L1 Variable name for the distance between the rib and the cooling pipe

L2 Variable name for the pitch distance between cooling pipes

LC1 Load Case 1 (Gravity load condition)

LC2 Load Case 2 (Thermal load condition)

POS Plasma Operating State

RELAP5-3D A specific thermal-hydraulic system analysis software code

SHELL181 Linear shell element type in ANSYS software

3. Project Facilities, Fusion Devices & Agencies

DEMO Demonstration Power Plant

DTT Divertor Tokamak Test

ENEA Agenzia nazionale per le nuove tecnologie, l'energia e lo sviluppo economico sostenibile (located in Frascati)

IEA International Energy Agency

ITER International Thermonuclear Experimental Reactor

JET Joint European Torus

JT-60 Japan Torus-60 (the predecessor facility)

JT-60SA Japan Torus-60 Super Advanced

T1 / T-15 Russian Tokamak experimental devices (T1 and T-15)

TFTR Tokamak Fusion Test Reactor

4. Materials, Chemistry & Nuclear Elements

AISI 316L American Iron and Steel Institute Grade 316L Stainless Steel

CO2 Carbon Dioxide

Co Cobalt (noted in chemical impurity limits)

D Deuterium

D-D Deuterium–Deuterium fusion reaction

D-T / DT Deuterium–Tritium fusion reaction

G10-CR A specialized cryogenic-grade glass-fiber reinforced epoxy composite

H Hydrogen

He Helium

Li Lithium

Li-6 Lithium-6 isotope

Li-Pb Lithium–Lead eutectic alloy coolant

SS 316LN Stainless Steel 316LN

SUS316L Steel Use Stainless Grade 316L (Japanese industrial standard)

T Tritium

U-235 Uranium-235 isotope

5. Units & Metric Indicators

°C Degrees Celsius

bar Unit of pressure

EJ Exajoules

G Gravitational acceleration force constant

g/s Grams per second (mass flow rate unit)

GW Gigawatts

ISO International Organization for Standardization

K Kelvin (unit of absolute thermodynamic temperature)

kg/m3 Kilograms per cubic meter (density unit)

MeV Megaelectronvolts

MJ Megajules

mm / cm / m Millimeters / Centimeters / Meters

MPa Megapascal (unit of pressure)

MW Megawatts

N4 / N6 ISO roughness grade classes

Q Fusion energy gain factor (ratio of fusion power to input power)

Ra Roughness average

W/m2 Watts per square meter (heat flux unit)

Glossary

Bellows Flexible, expandable connection pieces mounted between adjacent cooling pipe sections to allow them to contract freely under intense cryogenic cooling without forming localized peak mechanical stresses.

Blanket Heavy modules lining the internal walls of the vacuum vessel to catch high-energy neutrons, absorb kinetic heat for electricity generation, and breed tritium fuel using lithium interactions.

Bremsstrahlung Thermal braking radiation emitted when free-moving electrons are slowed down or deflected by positively charged ions within the plasma, causing energy loss.

Cryostat A vacuum-sealed, heavily insulated stainless-steel vessel that encloses the central reactor structure to isolate the cold superconducting components from warm ambient spaces.

Divertor The magnetic extraction system situated at the bottom of the vacuum vessel used to purge exhaust heat, impurities, and helium ash from the fusion plasma.

Labyrinth structure Overlapping, nested joint layouts on thermal shield panels that permit geometric displacement during thermal contractions or seismic events while keeping stray radiation blocked.

Stellarator A magnetic confinement fusion machine that shapes its plasma chamber using an intricate, twisted arrangement of external coils.

Tau (τ) The standard physics symbol representing the energy confinement time of plasma inside a reactor core.

Tokamak A magnetic confinement device shaped like a torus (donut) designed to trap high-temperature plasmas to achieve controlled nuclear fusion.

Tritium Breeding Ratio The metric measuring the efficiency of creating new tritium fuel inside the lithium blanket relative to the amount consumed by the core reactions.

von Mises equivalent stress A scalar value calculated from the stress tensor components used to predict the yielding threshold of ductile engineering materials under multidirectional load paths.